Eindhoven University of Technology

MASTER

Modelling lithium density in the plasma of Magnum-PSI

Machielsen, Mike

Award date:
2018

Link to publication

Disclaimer
This document contains a student thesis (bachelor's or master's), as authored by a student at Eindhoven University of Technology. Student theses are made available in the TU/e repository upon obtaining the required degree. The grade received is not published on the document as presented in the repository. The required complexity or quality of research of student theses may vary by program, and the required minimum study period may vary in duration.

General rights
Copyright and moral rights for the publications made accessible in the public portal are retained by the authors and/or other copyright owners and it is a condition of accessing publications that users recognise and abide by the legal requirements associated with these rights.

- Users may download and print one copy of any publication from the public portal for the purpose of private study or research.
- You may not further distribute the material or use it for any profit-making activity or commercial gain

Department of Physics
Fusion Research Group

Integrated Modelling and Transport

Modelling lithium density in the plasma of Magnum-PSI

Master Thesis

Mike Machielsen

Supervisors:
Hugo de Blank
Jan van Dijk
Peter Rindt

Eindhoven, 21 May 2018

Abstract

In order to handle the immense wall heat loads of future tokamaks ($\sim$ 10 MWm^{-2} steady state for ITER[1]) liquid lithium divertors are proposed. But an important question is whether core contamination due to excessive evaporation is acceptable.

In this work the multi-fluid model B2.5 has been used to model the plasma beam of the linear device Magnum-PSI. This machine can be used to study the physics of lithium transport in fusion relevant plasma. Modelling can help experiments in understanding the underlying physics of lithium transport. For the first the time the plasma beam of Magnum-PSI has been modelled throughout multiple chambers using the proper dimensions of the device.

Secondly, differential pumping is implemented into the boundary conditions of `B2.5`. The pressure prescribed as a BC in each chamber is found to be very important for the model result. The differentially pumped case gives higher temperatures than the regular case because there is less cooling by neutral H entering via the beam edge.

Thirdly, a validation with experiment is done for pure hydrogen plasma. The validation shows mixed results. In general agreement with experiments is poor, this is not unexpected due to the large Knudsen numbers for the neutral phase. Model predictions are of the same order of magnitude for 0.8 T and 1.2 T field strengths, but predict an electron temperature that is one order of magnitude too high for 0.4 T. For low gas flows ($\sim$ 6 slm) the model showed good agreement, but for higher gas flows the agreement is worse because the cooling is overestimated in the model.

Fourthly, lithium is added to the model. The model predicts the lithium density drops rapidly in axial direction, upstream the density is completely negligible. However, the upstream transport of Li outside of the beam is not taken into account. For higher evaporative fluxes the amount of lithium in the beam is obviously increased. But the Li^+ density in front of the target can be suppressed for fluxes exceeding about $10^{25}\,m^{-2}s^{-1}$ because of the lowered plasma temperature. Lithium is then ionized further upstream.

Finally, an unexpected result was observed in the differentially pumped case: The temperature was found to be higher, leading to more lithium ionization and consequently more redeposition. This leads to lower Li, Li^+ densities throughout the whole beam.

Contents

1 Introduction

People that consume more power have a higher quality of life on average. This seems to saturate at around 150 GJ per capita per year [2]. But a large part of the world is still below this level. As the world continues to develop, a large increase in energy consumption is expected. This is enhanced by the fact that the population is still growing. The U.S. Energy Information Administration predicts a 48% growth of the global energy demand in the period 2012-2040 [3]. The energy outlook report of MIT predicts the global energy demand to nearly double in 2010-2050 [4].

This means there is a need for new energy sources, more specifically, for sustainably ones. According to the Renewable energy & efficiency partnership this is defined as: "The provision of energy such that it meets the needs of the future without compromising the ability of future generations to meet their own needs" [5]. Nuclear fusion shows great potential to become one of these sustainable energy sources: There is enough fuel (deuterium) in the ocean to satisfy the world's electric energy needs for 150 billion years, assuming those needs remain at the level of 1995 [6]. Secondly, it is inherently safe because no nuclear runaway reaction is possible, compared to fission. Thirdly, fusion has in contrast to fission, no direct nuclear waste. The reactor itself though does become activated over its lifetime. Lastly, it is in principle CO_2-neutral[1]. It should be noted that nuclear fusion does not play a role in the energy transition, it is too late for that. The first demonstration plant is planned for operation in 2050, and that is just one reactor (or a few). However, this does not negate fusion's far future potential.

Nuclear fusion is the process in which multiple atomic nuclei fuse together. If the combined mass of the reaction products is smaller than that of the reactants, energy is released. The main candidate is fusion of deuterium (D) with tritium (T) because of its high reaction rate and deuterium availability: ${}^{2}_{1}\mathrm{D} + {}^{3}_{1}\mathrm{T} \longrightarrow {}^{1}_{0}\mathrm{n} + {}^{4}_{2}\mathrm{He} + 17.6\,\mathrm{MeV}$. Tritium is not found in nature, however the neutron that is released in the DT fusion reaction can be used to breed new tritium. The reaction products are captured by the wall and their kinetic energy is converted to heat. This heat can be used to turn water to steam. The steam is then used to drive a turbine and after that the power is converted to electrical via a generator[2].

The leading design of a nuclear fusion device is called a tokamak, see Fig. 1. This is a toroidal device built to magnetically confine a fusion plasma. Even though the plasma is magnetically confined, it can still "leak out" slowly. Eventually particles end up in the boundary layer after which they are quickly deposited on the wall. This happens at a narrow (≈ 1 cm radial width) strike zone on the bottom region of the wall [7]. The section of the wall around this strike zone is called the divertor, see Fig. 1.

[1] Of course this depends on the methods used in gathering resources.

[2] Other methods of energy conversion exist as well. For instance, concepts of fusion powered rockets usually envision using the helium ions directly as an ion thruster.

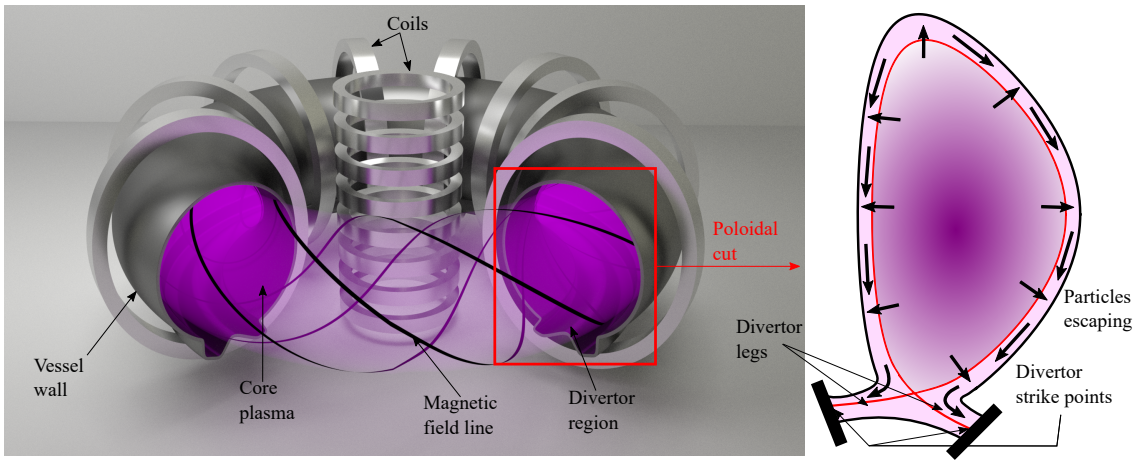

Figure 1: Schematic view of a tokamak, a poloidal cross section is examined in more detail on the right. The magnetic field lines are helical.

One of the issues when scaling up the design to a power plant level is the heat load on the wall, especially on the divertor. Predictions for the next big tokamak, ITER, show steady state heat loads of $\approx 10\,\mathrm{MWm}^{-2}$ on the divertor [8;9]. One of the proposed concepts to deal with the immense heat load on the wall of a tokamak is to use a liquid lithium divertor (LLD). LLDs have multiple advantages over solid divertors. In addition to heat transport by conduction, LLDs also have convection, evaporation and radiation. Furthermore, liquid lithium does not suffer from thermomechanical fatigue and it can be replenished. Also, the plasma is cleaner in some cases because the liquid can absorb some impurities [10]. Moreover, lithium has low Z so radiation losses in the core are limited. And lastly, LLDs can even improve confinement time [11;12]. However some types of LLDs suffer from splashing and excessive evaporation. If too much material is transported to the core it will cool down and dilute the core plasma. Some concepts aim to solve this contamination problem, such as the vapour box [13]. The vapour box is a differentially pumped vessel which holds liquid metal (such as lithium) in the bottom, see Fig 2.

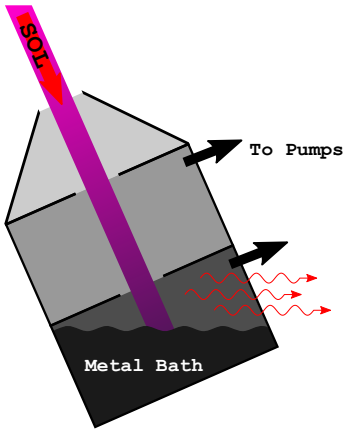

Figure 2: Poloidal cross section of a vapour box. This would be placed in one of the divertor legs such that the exhaust from the plasma enters as the pink beam. The boundary layer is also known as scrape-off layer, or SOL. In the bottom some liquid metal is present. Once evaporated, the metal can redistribute the heat via radiation. The box consists of multiple chambers that are individually pumped, this allows for different pressures in each chamber: differential pumping. This results in reduced lithium densities in higher chambers, as indicated by the shades of grey in each chamber.

Most of the evaporated material that enters the beam gets ionized, so neutrals have trouble entering or exiting through it. This is called "plasma plugging". The neutral particles also exchange momentum with the beam, meaning they are pushed back, again limiting the flux of neutrals that escape the vapour box. It is of great interest to find out how much lithium escapes the vapour box towards the plasma core, however testing this experimentally in a tokamak can be very expensive and complicated. So before testing the vapour box in a tokamak some modelling is in order. However, since no experimental data of a vapour box exists yet it is not possible to validate the results, instead a model will be made for the linear plasma device Magnum-PSI, stationed at DIFFER, Eindhoven. This device is also differentially pumped and operates in the same high density, low temperature regime as in the SOL of a tokamak. It is now being used to test liquid lithium divertor designs under ITER relevant conditions [14]. In the future also tests of vapour box prototypes are foreseen.

Modelling of the (transport of lithium in the) SOL requires a combination of fluid model for the plasma and a kinetic model for the neutrals. This is because of the long mean free path (mfp) of neutrals [15], as will be discussed in Section 2.2. Many of such codes have already been applied to linear devices in the past. `B2-Eirene` (also know as SOLPS) has been applied to the PSI-1 and PSI-2 linear devices [16]. These used the multi-fluid model `B2` to model the plasma in 2D and the 3D kinetic model `Eirene` for the neutrals. A newer version `B2.5-Eirene` has been used to model the linear devices Magnum-PSI and MAGPIE [17;18]. To model tilted targets a 3D treatment is required, this has been done for the device MPEX with `EMC3-Eirene` [19]. A model similar to `B2.5-Eirene`, named `SolEdge2D-Eirene` has been used to model the device Pilot-PSI [20]. Also a fluid model of the expansion of plasma in the linear device Magnum-PSI exists, using the model `PLASIMO` [21]. `Eunomia` is a variation on the kinetic model `Eirene`, specifically designed for linear devices. Furthermore, `B2.5-Eunomia` has been used to model hydrogen plasmas in Pilot-PSI [15]. Recently, modelling of lithium in Magnum-PSI has been done using `Eunomia` [22]. It is of interest to see if the code `B2.5` can be used to model a vapour box. Therefore in this project lithium is implemented in `B2.5`. Implementation of lithium in the coupled model `B2.5-Eunomia` is also being worked on, but is not within the scope of this thesis.

1.1 Research question

The main research question is: "*How is the lithium that comes from a liquid target in Magnum-PSI re-distributed over the plasma ?*"

There are several factors that affect the global particle balance: for neutral lithium there is a source of evaporation at the target, a sink due to ionization, thirdly Li is not confined to the magnetic field so it can leave the beam domain via the beam edge, and lastly it can leave upstream at the source. For Li^+ a source exists due to ionization of Li, a sink due to diffusion of lithium ions through the beam edge, Li^+ that leaves the domain via the source, and finally Li^+ that is redeposited on the target. The diffusion is probably not very significant since the distance between source and target is only about a metre. To investigate the importance of each of these factors several additions to the numerical model of Pilot-PSI need to be made: The geometry will be adapted to that of Magnum-PSI. Secondly, differential pumping will be implemented as a new boundary condition. This leads to the first subquestion:

- "*Is it possible to model differential pumping in* `B2.5`*?*"

Using this boundary condition a validation with experiment will be done for the pure hydrogen case. Thirdly, neutral lithium, and singly ionized lithium[3] will be added to the model as separate fluids. This results in the following subquestions:

- "*Can the lithium density be modelled with* `B2.5` *for Magnum-PSI?*"
- "*What is the effect of differential pumping on the lithium density in Magnum-PSI?*"

Finally, the maximum allowed lithium efflux at the plasma source can put a limit on the evaporation rate. This raises another question:

- "*How does the lithium density near the plasma source depend on the evaporation rate?*"

In Chapter 2 the relevant theory will be discussed, including the fluid equations, physical processes and the coordinate system of the model. The numerical method and experimental set-up are introduced in Chapter 3. Results of the pure hydrogen model are presented in Chapter 4, including differential pumping and an experimental validation. The discussion on those results is found in Chapter 5. A plasma including lithium will be addressed in Chapter 6, also the effect of differential pumping is investigated for a lithium case and the evaporation flux is varied. And the accompanying discussion in Chapter 7. Finally the conclusion is found in Chapter 8.

[3] No Li^{2+} or Li^{3+} will be taken into account because they are not very abundant at typical plasma temperatures of 4 eV.

2 Theory of a magnetized plasma beam

In this chapter the main fluid equations of B2.5 will be introduced, the applicability will be discussed, followed by the coordinate system and finally the physics processes in B2.5 are discussed.

2.1 Fluid equations

The fluid model of B2.5 relies on three conservation principles: conservation of particles, momentum and energy. The equations in this Section will present these principles, accompanied by some auxiliary equations. In the simulations a multi-fluid plasma will be used, but for simplicity the equations (3)-(5) are limited to a plasma with just one ion species. For the full multi-fluid equations (in generalized coordinates) see the SOLPS manual [23] or Refs. [24;25;26]. The continuity equations are

$$\frac{\partial n_i}{\partial t} + \nabla \cdot \mathbf{\Gamma}_i = S_{n_i} \tag{1a}$$

$$\frac{\partial n_e}{\partial t} + \nabla \cdot \mathbf{\Gamma}_e = S_{n_e} \tag{1b}$$

With n the number density, $\mathbf{\Gamma}$ the particle flux and S_n a source term. The subscript i indicates ions in all the equations in this section. Electrons are indicated with subscript e. Due to charge conservation the following relation exists for the sources: $S_{n_e} = \sum_a S_{n_a} Z_a$, with a the ion species and Z_a the charge state. Another very good approximation is local quasi-neutrality: $n_e = \sum_a n_a Z_a$. This means that Eq. (1b) does not need to be solved anymore, so also no boundary condition needs to be specified for electron density. Subtraction of the continuity equations yields the total continuity equation: $\nabla \cdot (\sum_a n_a Z_a \mathbf{v}_a - n_e \mathbf{v}_e) = 0$, or

$$\nabla \cdot \mathbf{j} = 0 \tag{2}$$

so the current density $\mathbf{j}$ is divergence free. The momentum balance of the ion fluid is

$$\frac{\partial}{\partial t}\left(m_i n_i \mathbf{v}_i\right) + \nabla \cdot \left(m_i n_i \mathbf{v}_i \mathbf{v}_i\right) = -\nabla p_i - \nabla \cdot \mathbf{\Pi}_i + Z_i e n_i \left(\mathbf{E} + \mathbf{v}_i \times \mathbf{B}\right) + \mathbf{R}_i + \mathbf{S}_{m_i \mathbf{v}_i} \tag{3a}$$

With m the particle mass, $\mathbf{v} \equiv \mathbf{\Gamma}/n$ the velocity of a species, p the partial pressure, $\mathbf{\Pi}$ the viscosity tensor, $\mathbf{E}$ the electric field, $\mathbf{B}$ the magnetic field, $\mathbf{R}$ the friction term and $\mathbf{S}_{m\mathbf{v}}$ a momentum source due to reactions. The magnetic field is assumed to be constant. The viscosity tensor is the part of the pressure tensor that follows from the anisotropy of the particle distribution function. The friction is in general different for each species, it is the sum of the friction with electrons and all ion species except for the species in question. For the direction parallel to the magnetic field the momentum balance (3a) is used, in perpendicular direction a simple Fick diffusion law is used. Typically anomalous diffusion coefficients are used that best fit tokamak experiments, see Section 4.1.1. A similar momentum balance holds for electrons, if electron mass is neglected the following expression is obtained

$$-\nabla p_e - e n_e \left(\mathbf{E} + \mathbf{v}_e \times \mathbf{B}\right) + \mathbf{R}_e = 0 \tag{3b}$$

This is sometimes referred to as generalized Ohm's law. The friction term is

$$\mathbf{R}_e = -\mathbf{R}_i = e n_e \left(\frac{\mathbf{j}_\parallel}{\sigma_\parallel} + \frac{\mathbf{j}_\perp}{\sigma_\perp}\right) - 0.71 n_e \nabla_\parallel \hat{T}_e - \frac{3}{2}\frac{e n_e^2}{\sigma_\perp B^2}\mathbf{B} \times \nabla \hat{T}_e \tag{3c}$$

Where $\parallel$ means parallel to the magnetic field, and $\perp$ means perpendicular to the magnetic field. See Section 2.3 for an illustration of these basis vectors. The electrical conductivity is indicated with σ, the elementary charge with e. The thermodynamic temperature is indicated with T, but 'temperature' in energy units refers to the the velocity space average $\hat{T} \equiv m \left\langle |\delta \mathbf{v}|^2 \right\rangle /3$ with $\delta \mathbf{v}$ the velocity deviation of a particle with respect to the mean velocity. This is customary in the

field of fusion and $\hat{T}$ is also defined outside of thermal equilibrium, however in thermal equilibrium $\hat{T} = k_B T$ with k_B the Boltzmann constant. The part enclosed by parentheses in Eq. (3c) is due to a relative macroscopic velocity between electrons and ions. The work done by this friction term is known as ohmic heating, or Joule heating. The value 0.71 is a numerical coefficient derived for singly ionized ions, see Ref. [26].

The parallel current can be determined from Eqs. (3b),(3c), namely, $\mathbf{v}_e \times \mathbf{B}$ does not have a parallel component. The electron velocity is extracted from the definition of current density $\mathbf{j} = e\left(\sum_a Z_a n_a \mathbf{v}_a - n_e \mathbf{v}_e\right)$, so

$$\mathbf{v}_e = \frac{1}{n_e}\left(\sum_a Z_a n_a \mathbf{v}_a - \frac{\mathbf{j}}{e}\right) \tag{3d}$$

Hence also Eq. (3b) need not be solved.
The energy balance for ions is given by

$$\frac{\partial}{\partial t}\left(\frac{3}{2} n_i \hat{T}_i + \frac{m_i n_i}{2} v_i^2\right) + \nabla\cdot\left[\left(\frac{5}{2} n_i \hat{T}_i + \frac{m_i n_i}{2} v_i^2\right)\mathbf{v}_i + \mathbf{\Pi}_i \cdot \mathbf{v}_i + \mathbf{q}_i\right] = (e n_i Z_i \mathbf{E} + \mathbf{R}_i)\cdot\mathbf{v}_i - Q_{ei} + S_E^i \tag{4a}$$

The first parentheses on the left hand side (l.h.s.) enclose the total energy density of the ions: internal and kinetic energies. Enclosed by the square brackets is the energy flux: due to macroscopic flow with velocity $\mathbf{v}$, work done by viscous stress, and finally the heat flux $\mathbf{q}$. Viscosity always leads to dissipation, thus increase of internal energy. The heat flux, and energy transport by advection redistribute the energy, but do not generate it. On the right hand side (r.h.s.) there is work done by the electric field, this converts potential energy into kinetic energy. This is not a heating term because it does not alter the internal energy directly. The term $\mathbf{R}\cdot\mathbf{v}$ generates heat via friction. Then, Q is the heat exchange due to collisions with other species, this does not generate heat. And finally, S is an energy source due to various processes: ionization, recombination, radiation, etc. For electrons

$$\frac{\partial}{\partial t}\left(\frac{3}{2} n_e \hat{T}_e\right) + \nabla\cdot\left(\frac{5}{2} n_e \hat{T}_e \mathbf{v}_e + \mathbf{q}_e\right) = -e n_e \mathbf{E}\cdot\mathbf{v}_e + \mathbf{R}_e\cdot\mathbf{v}_i + Q_{ei} + S_E^e \tag{4b}$$

The heat fluxes $\mathbf{q}_e$ and $\mathbf{q}_i$ from Eqs. (4) are given by

$$\mathbf{q}_i = -\kappa_\parallel^i \nabla_\parallel \hat{T}_i - \kappa_\perp^i \nabla_\perp \hat{T}_i + \kappa_\times^i \frac{\mathbf{B}}{B} \times \nabla_\perp \hat{T}_i \tag{5a}$$

$$\mathbf{q}_e = -\kappa_\parallel^e \nabla_\parallel \hat{T}_e - \kappa_\perp^e \nabla_\perp \hat{T}_e - \kappa_\times^e \frac{\mathbf{B}}{B} \times \nabla_\perp \hat{T}_e - 0.71 \frac{\hat{T}_e}{e}\mathbf{j}_\parallel - \frac{3}{2}\frac{\hat{T}_e}{e\omega_e \tau_e B}\mathbf{B}\times\mathbf{j}_\perp \tag{5b}$$

With κ the thermal conductivity. See Ref. [27] for a detailed explanation of each term in the equation.

2.2 Purpose and applicability of B2.5

`B2.5-Eunomia`[4] is a code package which is already used in the past to model the linear plasma device called Pilot-PSI [15]. It is a combination of the 2D plasma fluid model `B2.5` and the 3D kinetic neutral model `Eunomia`. The reason for this combination of two codes is the limited applicability of the fluid model. It is applicable as long as the distribution function is allowed to relax to a Maxwellian [26]. Therefore the macroscopic quantities should change 'slowly', both in time and space. Relaxation happens through collisions, so the relevant time scale is the collision time τ, and the relevant length scale is the mean free path λ. In this project only the equilibrium

[4] Version `01.001.027` of `B2.5` is used.

state is studied, so there is no variation in time. The distance over which a quantity ξ changes significantly is defined as $L \equiv \xi / |\nabla \xi|$. For neutral particles the following should hold $\lambda \ll L$. The Knudsen number (Kn) is defined[5] as the mean free path over a characteristic length scale: $\mathrm{Kn} \equiv \lambda / L$, so the requirement is often written as $\mathrm{Kn} \ll 1$.

However, for charged particles, and given there is a magnetic field, L splits into $L_\parallel \equiv \xi / \left|\nabla_\parallel \xi\right|$ and $L_\perp \equiv \xi / |\nabla_\perp \xi|$. Transport of charged particles perpendicular to the magnetic field is bounded by the Larmor radius ρ_L, so the requirements are $\lambda \ll L_\parallel$ and $\rho_L \ll L_\perp$. With $\rho_L / \lambda \approx 1/(\omega\tau)$ and ω the Larmor frequency. This means the requirement in perpendicular direction is somewhat relaxed because in a magnetized plasma $\omega\tau \gg 1$.

Suppose the plasma density in the beam is normally distributed, then the typical perpendicular length scale is the standard deviation, σ. With $L_\perp = \sigma \approx 10$ mm. Secondly, the worst case scenario (maximum) for the Larmor radius is 0.30 mm for Li^+. Thirdly, the parallel connection length is about a meter, therefore also $L_\parallel$ is of the order of 1 m.

Typically in plasmas charged particle collisions are far more prevalent than neutral-ion collisions because of the long range interaction of the Coulomb force. Furthermore, the electron population and ion population reach equilibrium much faster independently, than together. So only ion-ion collisions will be considered in this analysis. The mean free path for these collisions depends on the density and temperature [28], plugging in typical values reveals λ ranges from a few micrometer to several millimetres. So in Magnum-PSI the Knudsen number is small for ions, $\mathrm{Kn}_\parallel \ll 1$, and $\rho_L \ll L_\perp$ are satisfied. The thermal velocity of electrons is about $\sqrt{m_i/m_e}$ times that of ions and the electron-electron collision time is smaller by the same factor, so their mfp is comparable to that of ions. Their Larmor radius is smaller, $\rho_{L,e} \approx \rho_{L,i}\sqrt{m_e/m_i}$, so certainly the electrons can be modelled as a fluid.

However, strong gradients are expected just in front of the target, meaning the axial gradient length may be far smaller than expected. (The plasma sheath is not meant to be resolved, but even outside of the sheath strong gradients can exist). Previous experimental and modelling efforts hint at this: For exponential decay of the density as function of distance to the target, the gradient length equals the decay length, which was found to be 3-4 mm for neutral lithium. See Ref. [22], p. 44. This is much smaller than the length scale $L_\parallel$ for ions.

Finally, the neutrals do not have long range interactions and do not gyrate. Their mfp can be a few centimetre or more [22;15] so the gradient length is easily exceeded. This is problematic for the neutral phase, $\mathrm{Kn} \gtrsim 1$, so it cannot be approximated as a fluid. For this reason a kinetic model is typically used to model the neutral phase [29], such as `Eunomia`. However, as already mentioned in the introduction, due to time constraints a neutral fluid model is used in this work.

2.3 Coordinate system

`B2.5` uses field-aligned orthogonal coordinates, which is in general described by an orthogonal curvilinear coordinate system. The directions are parallel, diamagnetic and radial. The practicality of this choice already became clear in Section 2.1 due to the anisotropy of the equations. But because azimuthal symmetry is assumed, a different coordinate system is more practical. Namely, the system consisting of the parallel (but confined to a radial plane), azimuthal and radial directions, see Fig. 3. The azimuthal coordinate can be ignored reducing the model to 2D. The transformation between the two coordinate systems is already contained in `B2.5`.

[5] Note that the Knudsen number varies, based on the choice of ξ. Often density, temperature or magnetic field strength are chosen for ξ. In some literature a geometric length such as diameter of the vessel is chosen as characteristic length.

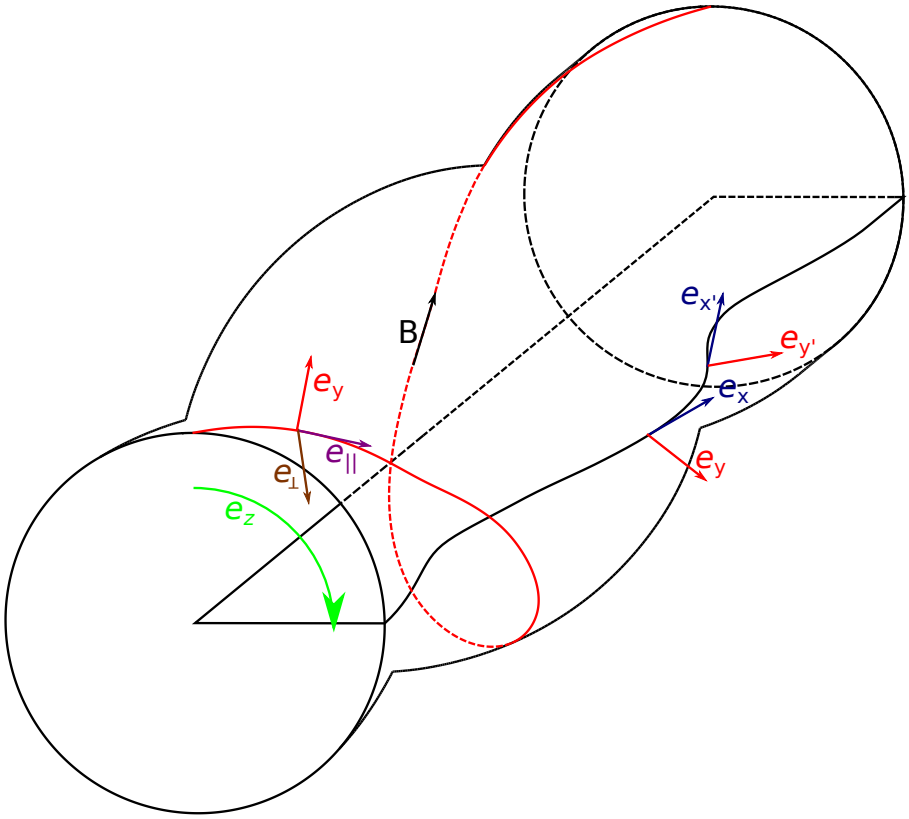

Figure 3: Coordinate system in cylindrical geometry is shown, with one radial slice highlighted.In general the cylindrical shape (envelope) can bulge out and the field can have an azimuthal component. To be able to see it this is greatly exaggerated, in Magnum-PSI these effects are negligible. Some linear devices without superconducting coils can show significant bulging, but in principle the code can handle such geometry. The vector $e_\parallel$ points along the magnetic field, $e_\perp$ is perpendicular to the field, but tangent to the envelope, and e_y is perpendicular to both. The e_x direction points along the projection of $e_\parallel$ on a radial plane. Note that e_x does not perfectly align with the axial direction, and e_y is not perfectly normal to the axis. The coordinates have been drawn again at a different position, x', y', z'.

The coordinate symbols in Fig. 3 are the same as in the code. However, since `B2.5` is designed for tokamaks, in the code they are known as x (poloidal), y (diamagnetic) and z (toroidal).

2.4 Physics processes in B2.5

`B2.5` can run in stand-alone mode, or it can be coupled to a kinetic model such as `Eirene` or `Eunomia`,[18;15]. For simplicity only the stand-alone mode will be used. This means the neutral phase is modelled as a fluid, just as the ion/electron fluids from Sect. 2.1 with the same temperature as that of the ions. Except for the fact that this neutral phase is not carrying charge. Thus its behaviour is not influenced by the electric or magnetic fields and it does not carry current. Of course this can introduce problems since the Knudsen number is larger than unity for neutrals, as indicated in the introduction.

Since a fluid model is used particle collisions are not modelled, but they are included indirectly. Namely, via friction between different fluid phases. The fluids can move through each other so at each position in the plasma there can be friction. Work done by this friction heats the plasma, see Section 2.1. Furthermore, the fluids can also exchange energy if there is a temperature difference.

Moreover, the ADAS database is used which contains rate coefficients for ionization, recombination, charge exchange (CX) (in $\mathrm{cm^3 s^{-1}}$) and line radiation, bremsstrahlung (in $\mathrm{Jcm^3 s^{-1}}$). The possible dependence on electron temperature and electron density is included. CX between Li and Li^+ is neglected because of the low density of lithium throughout most of the plasma beam. Also this reaction does not change the total amount of lithium in the plasma. Furthermore CX between lithium and hydrogen is neglected, because the rates are dwarfed by recombination/ionization, as concluded by T. Abrams,[30]. Lastly, at the moment of writing, the ADAS database only has CX rates with deuterium as the donor atom. Therefore the CX rates of hydrogen ($H + H^+ \longrightarrow H^+ + H$) are overwritten by the amjuel database from 2017, Section 3.19 [31]. The beam energy is 'crudely' assumed to be $0.5 m_p (v_p - v_H)^2 \approx 0.1\,\mathrm{eV}$, with v_p the typical bulk velocity of ions, the neutral hydrogen is assumed to be immobile. The log of the rate coefficients is linearly interpolated on a 2D mesh: $\log(\hat{T}_e(\mathrm{eV})), \log(n_e(\mathrm{cm^{-3}}))$. If the temperature is out of the tabulated range linear extrapolation is used, if however the electron density is out of range, a constant value is assumed. For more info on ADAS, see http://www.adas.ac.uk/about.php. Finally, sputtering, evaporation, recycling and secondary electron emission can also be enabled, this is set in the input files of B2.5 itself.

2.4.1 Lithium erosion

The lithium surface erodes over time due to sputtering and evaporation. At the relevant temperatures of about 900 °C [32] evaporation dominates over physical and chemical sputtering [33]. At the edges of the target the temperature is lower, and sputtering dominates. However the incoming plasma flux is less intense there. But the the evaporation scales very strongly with temperature, so the total erosion losses are still dominated by the evaporation from the centre. So only evaporation is considered here as a loss mechanism, see Fig. 13. The Hertz-Knudsen equation evaporation equation is used

$$\Gamma_{evap} = \frac{P_{vap} - P_a}{\sqrt{2\pi m_{Li} \hat{T}_{plate}}} \tag{6}$$

With P_a the partial ambient pressure of lithium in the plasma above the target. Usually an empirical formula is used for the vapour pressure. The following formula is used for lithium [34]

$$P_{vap}[\mathrm{Pa}] = \exp\left(26.89 - 18880/T_{plate}[\mathrm{K}]\right) \cdot T_{plate}[\mathrm{K}]^{-0.4942} \tag{7}$$

For simplicity the ambient partial pressure of lithium is neglected, hence a constant boundary condition can be employed (no feedback needed from the plasma state).

B2.5 only models up to the magnetic pre-sheath edge [35], so any redeposition taking place in the in the magnetic pre-sheath and the sheath is not taken into account in the model. If this is significant the evaporation BC ought to be corrected for this. However, the ionization length of Li in a typical divertor environment is about 5 mm [36], but the sheath and pre-sheath are much thinner. Typically, the sheath thickness is of the order of a Debye length [6], so 1 micron. The magnetic pre-sheath has thickness of the order of a ion Debye length [38;39], so about 0.1 mm. Gyro orbits that intersect with the target can also cause immediate redeposition, however only cases with a magnetic field normal to the target are modelled so this does not apply. Therefore the evaporation rate does not need to be corrected for such immediate redeposition.

Tests have been conducted before with deuterium plasma on a thin lithium surface (tens of microns) in Magnum-PSI, and the lithium was found to saturate with deuterium in 5-10 seconds, see Ref. [40]. Secondly, in experiments of PISCES-B with deuterium on liquid lithium, the deuterium density was found to be 1:1 for D:Li. So it is safe to assume a lithium-deuteride layer forms

[6] In unmagnetized plasmas, or cases where the magnetic field strikes the target under an angle the sheath thickness is roughly a Debye length [37;25], for $\hat{T}_e$=1 eV, n_e=$10^{20}\mathrm{m^{-3}}$ this is about one micrometre.

on top of the liquid lithium. Because of this, sputtering of lithium is less effective, but also the evaporation rate was found to be drastically diminished, compared to pure lithium. The authors estimate a pure LiD surface to erode with just one twentieth of the rate that pure lithium does (at 600 °C-700 °C in NSTX-U). T. Abrams presents a formula for the reduction of lithium vapour pressure for a LiD substrate, stating "this reduction is effectively independent of temperature" [30]. So even at target temperatures of 900 °C the evaporative flux of lithium may be overestimated. Lastly, because the lithium surface is saturated within seconds, the hydrogen recycling rate is set to 1 at the target, see Section 4.1.1.

3 Computational approach & experimental set-up

3.1 Numerical method

B2.5 uses a finite volume method (FVM). FVMs solve the integral form of the equations in Section 2.1. This means the quantity of interest is total/ integrated flux (...s^{-1}), not flux (...$s^{-1}m^{-2}$) as in finite difference methods. FVMs are a good choice for modelling conservation laws since the influx on one cell face equals the outflux of the neighbour cell on that same face. The four main equations from Sect. 2.1: conservation of particles (1a), momentum (3a) and energy (4a),(4b), can be cast in an advection-diffusion form: $D(\Phi) = \partial(\Phi)/\partial t + \nabla \cdot (\mathbf{v}\Phi - \boldsymbol{\kappa} \cdot \nabla\Phi) - S = 0$,[24]. Where D is the operator, Φ is the quantity of interest (n, $nm\mathbf{v}$ or $(3n\hat{T} + mnv^2)/2$), S is the source. And in general $\boldsymbol{\kappa}$ is a tensor that describes transport by diffusion.

Several numerical schemes that can solve this type of equation are available in B2.5: The upwind scheme , the hybrid difference scheme and the power law scheme[7]. The choice of numerical scheme is determined by the Péclet number (Pe), which gives the ratio between advective transport and diffusive transport. For $|\mathrm{Pe}| \gg 1$ the upwind scheme is a good choice, for $|\mathrm{Pe}| \ll 1$ the central difference scheme is better. The hybrid scheme works for any value of the Péclet number since it combines best of the the upwind and central difference schemes: for $|\mathrm{Pe}| \leq 2$ it is equal to the central difference scheme, and for $|\mathrm{Pe}| > 2$ it is identical to the upwind scheme. That is why B2.5 uses the hybrid scheme. The schemes only differ in their approximation of the cell face value of Φ.

Independent of that, discretization is fully implicit in time for each equation. The general procedure is to use one of the schemes to discretize the differential equations, set up a sparse matrix equation and then solve this via an iterative method. This means an initial value Φ' is used, for which $D(\Phi') = -R$ holds, with R the residual. For the solution Φ the following holds $D(\Phi) = 0$, so for the error $\Phi - \Phi'$ this is true: $D(\Delta\Phi) = R$. Iteration minimizes the residual. Note that B2.5 is time-dependent, but uses pseudo time-stepping. This means that time steps are actually iterations used to march towards the steady state solution. These 'artificial' time steps are a kind of relaxation parameter. Therefore the solution at intermediate time steps is not relevant and does not need to be realistic. Furthermore, the grid of B2.5 is 2D and spans a radial slice of Magnum-PSI, hence cylindrical symmetry is assumed, see Fig. 6.

3.1.1 Boundary conditions

Boundary conditions (BCs) are implemented by means of 'ghost cells' (also known as 'guards cells' or 'boundary cells'). These are additional cells that are tacked on the edges of the physical domain, see Fig. 4. Within these cells sources/sinks are placed to guarantee a certain flux through their boundaries. This can be used to set several different kinds of BCs.

[7] The power law scheme provides a slight upgrade to the hybrid scheme in accuracy, but it is more expensive as well. It is exclusively used for the momentum balance.

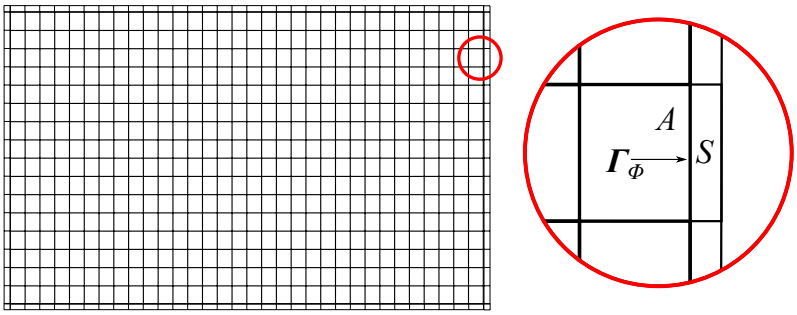

Figure 4: Illustration of the ghost cell principle, in this sketch the physical domain is 32×16 cells, but with the ghost cells this becomes 34×18. An enhanced view is seen on the right. With A the boundary area, S the ghost source and Γ_Φ the flux of some quantity Φ. Figure based on Ref. [24].

There is an array of different boundary conditions to choose from, such as: Dirichlet, Neumann, decay length and sheath BCs. Although these are different to the user, the code converts these to sources/sinks in the ghost cells. For most of the BC types a homogeneous value can be set, a profile, or some expression based on plasma parameters. To illustrate how these boundary conditions apply two examples will be given:

- Suppose a density n_b is desired on the north boundary. A particle source is placed in the ghost cells on the north boundary: $S_n = VA(n_b - n)$, with A the area of the ghost cell facing south, n the density in the ghost cell and V some velocity. In the time evolution this will result in negative feedback: if n is too high, $S_n < 0$ so the density drops, if n is too low, $S_n > 0$ and n will rise. V is not a physical velocity, it is just a pre-factor that is set in the code to speed up convergence. It is chosen to be 'large' ($V \approx 10^{13}$ m/s) on purpose such that $|S_n|$ is 'large' and thus the density will converge 'fast'. However, it cannot be set too large otherwise it will cause much overshoot.
- Suppose the derivative of the potential is specified on the south boundary. Let $C \equiv \frac{\partial \phi}{\partial y} = \frac{\phi_N - \phi_b}{\Delta y}$, with ϕ_N the potential in the north neighbour cell, and Δy the inter cell distance. Now ϕ is not set directly, always via a source: $S_{ch} = VA(\phi_b - \phi)$. Using the expression for C this yields $S_{ch} = VA(\phi_N - C\Delta y - \phi)$. The value of the charge source S_{ch} will oscillate until it converges on 0.

The BCs are defined in the `B2.5` subroutine `b2stbc_phys.f`. For further info the reader is directed to the write-up in Refs. [24;23].

On each boundary in the geometry a BC has to be set for the: electron temperature, ion temperature, neutral densities, ion densities, neutral parallel velocities, ion parallel velocities and the electric potential. The perpendicular velocities are calculated explicitly from a diffusion equation and don't need BCs. Secondly, the electron density and electron velocity are determined from the ion density and ion velocity respectively, so also do not require a BC. Finally, in the model only one ion temperature is used for all ion (and neutral) species. This is a reasonable assumption since the temperatures are tightly coupled via charge exchange. So in general a total of $N_{BC}(3 + 2N_s)$ BCs are required, with N_{BC} the number of boundaries and N_s the number of species [8]. The specific BCs depend on the situation, see Sections 4.1, 6.1 for the choices concerning hydrogen and lithium respectively.

[8] Although, it is possible to set no BC at all. The ghost cell sources are then just left at their initial value, which is zero. This is effectively a zero flux BC.

3.2 Magnum-PSI

Magnum-PSI is a linear plasma device for testing plasma surface interactions in fusion relevant circumstances. It is located at DIFFER, Eindhoven, The Netherlands. Its purpose is to investigate the interaction between materials and a low temperature, high density plasma that is typical for the divertor environment. Especially aiming at long, high power, high fluence plasma exposures. The linear geometry allows for improved reproducibility, flexibility and diagnostic access compared to a tokamak.

Magnum-PSI utilizes a cascaded arc plasma source to produce a high density $\sim 10^{20}\mathrm{m}^{-3}$, low temperature (a few eV) plasma, see Ref. [41]. A magnetic field (up to 2.5 T) is used to confine the plasma, but it also improves source efficiency since charge carriers are less likely to flow directly to the opposite electrode. An image of Magnum-PSI is seen below.

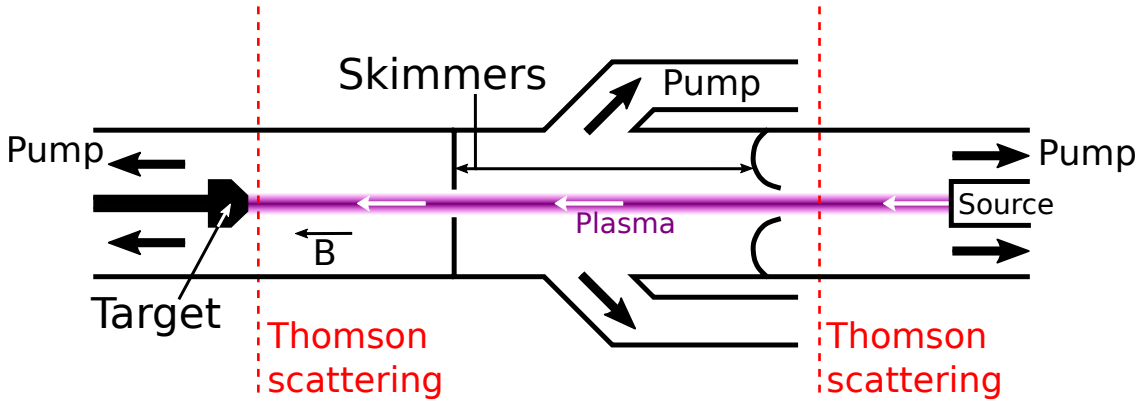

Figure 5: Schematic drawing of Magnum-PSI, a radial cross section is depicted. On the right there is the plasma source, on the left the target. The multi target holder is shown which has five mounting faces. The vessel is divided into three chambers, from left to right the target, heating and source chamber. Superconducting coils wrap around the device to create the axial magnetic field.

The plasma beam is heated via ohmic heating [42]. The three chambers are separated by skimmers, and are individually pumped. This means a different pressure in each chamber can be maintained: a.k.a. differential pumping. Typical pressures are 0.25 Pa, 0.4 Pa and 2 Pa in the target, heating and source chamber respectively. These pressures can be varied by adjusting the pumping rate in each chamber, also gas puffing is available in the target chamber.

3.2.1 Grid for Magnum-PSI

The grid of Magnum-PSI is calculated using the program `b2grid`. Based on the positions of the coils and the number of windings and layers it calculates the magnetic field lines. The influence of the vessel and plasma is neglected, $\mathbf{B}$ does not depend on time either. Then a set amount of radial lines are drawn. The intersection points of the radial lines with the field lines form the corner positions of `B2.5`'s grid, see Fig. 6. From here on the symbol z will denote the distance along the axis of the device, and r the radial distance from the axis.

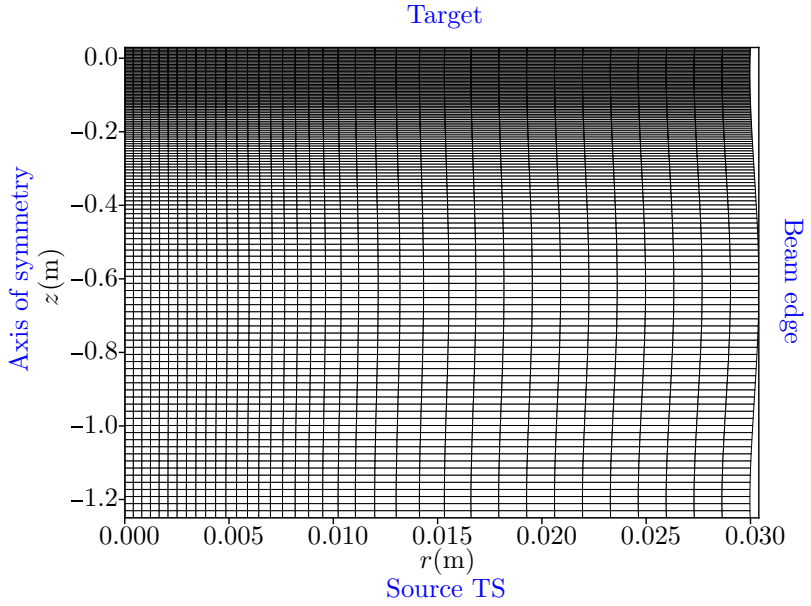

Figure 6: The grid used to model Magnum-PSI. The core of the plasma beam is on the left side, the outboard side is on the right. The target is located at the top edge, and the plasma source Thomson scattering (TS) location at the bottom. Strong gradients exist near the target so the cells are made smaller to be able to resolve this. The distance between the plasma source and the target is about 1380 mm, depending on the variable position of the target and source. The target chamber TS position is located at $z = 0$. The size of the grid is 36×128 cells ($N_r \times N_z$). This resolution is used unless specified otherwise.

The grid in Fig. 6 spans from just in front of the source to the target. The main reason to start "just in front" is that `B2.5` is not suited to model the expansion zone of the plasma[21] since the transport coefficients are derived for a magnetized plasma ($\omega\tau \gg 1$). The second reason is that the Thomson scattering (TS) measurement, required for the inlet boundary condition, is conducted a few centimetres in front of the source. This grid corresponds to a field strength of 0.8 T and is used for all simulations, except for some in the validation section, see 4.3. Also field strengths of 0.4 T and 1.2 T are investigated, so those grids are slightly more/less curved. Secondly, in Appendix A.1 a model of just the target chamber is used, which also has a different grid of course.

Furthermore, a grid radius of 3 cm is used since that equals the radius of the target. However the skimmers slightly protrude into this domain because the skimmer hole has a radius of 2.5 cm. This geometrical feature is neglected, which is not a big infraction because the electron density decays rather fast. E.g. in the inlet profile of the discharge from Section 4.2 n_e at $r = 2.5$ cm is already less than 10^{-3} times the peak value. Also the current density at $r > 2.5$ cm is negligible, see Fig. 22. The important effect of skimmers on the neutral pressure is taken into account via the boundary condition, see Section 4.1.

4 Modelling pure hydrogen discharges in the full plasma volume of Magnum-PSI

4.1 Boundary conditions for hydrogen

The boundary conditions are specific for each run, here the ones associated with the pure hydrogen (atomic species H, H^+) modelling are introduced. Note that sometimes the value of a quantity has been set, sometimes the flux, or something else. E.g. it is possible to set the temperature, or the energy flux, or even the decay length of the temperature profile at the boundary. That is possible because the code translates all of these to a heat source or sink in the ghost cells, see Section 3.1.1.

- Core side:
  - No BC is set for the electric potential.
  - Both the electron and ion energy fluxes have been set to zero.
  - The particle fluxes have been set to zero.
  - Also the parallel momentum fluxes are zero.

  Since axisymmetry is assumed, no net flux crosses the core side. To be clear, the potential is not set to zero, but there is no BC applied for the electric potential. This means the ghost cell sources are zero, and thus the current through the core surface is zero.

- Outboard side:
  - No BC is set for the electric potential.
  - The electron temperature is set to 0.5 eV.
  - For the ion temperature a decay length of 3 cm has been used.
  - The neutral density is set, based on a measured pressure.
  - For the ion density a decay length of 3 cm is chosen.
  - The parallel momentum fluxes are set to zero.

  Again no BC is set for the potential, that is fine because the radial current is negligible compared to the parallel current anyway. Density and temperature drop off in radial direction. A decay length of 1 cm is typically chosen at the outboard side[43;18;16;44], here 3 cm is chosen because that is roughly the beam radius. In the code this is actually a way of setting the gradient of these quantities, thereby a certain outflux is enforced. The specific value of this decay length was found not to be that important. Ion density decay lengths of 1 m and 10^{-4} m were also investigated, but the final plasma state was nearly identical[9]. That is because the main ion loss is still at the target, see Appendix A.2.

  The neutral density is set based on the partial pressure, using the ideal gas law: $n = P/\hat{T}_i$. The pressure is typically 1 Pa, but depends on the experiment in question. However, this pressure is measured at the wall of the device, not the beam edge. The first assumption is that the neutral population outside of the beam is dominated by hydrogen, so the partial pressure of hydrogen equals the total measured pressure at the wall. Secondly, the neutral volume outside of the beam contains no plasma and is therefore not confined. Hence, the pressure equilibrates and the pressure should be homogeneous in this outer volume.

[9]The ion density was found to be about 4% smaller on average for the case with a 10^{-4} m decay length, compared to the case with a 1 m decay length. There are a few outlying cells, but note that the variation in decay length is four orders of magnitude. The studied case contained the species H, H^+, Li, Li^+.

There is one issue with this kind of BC, it is found to be unstable in combination with decay length BCs for the temperature. This is possibly explained as follows: If for instance the temperature rises, more neutrals will ionize, which means less line radiation, thus an even higher temperature. If the boundary value of the neutral density would be fixed this BC would supply extra neutrals to compensate. However due to the pressure BC, the pressure is fixed instead of the density. When the temperature goes up, the boundary value of the density drops, so this is a positive feedback loop. The opposite could also happen, a lower temperature in the ghost cells causes a higher neutral density, even more line radiation, so even lower temperature, etc. The feedback loop does not continue forever, for instance if the temperature goes up, also the heat loss to the outboard side increases, but this is not enough. A way to fix the issue is to pin at least one of the temperatures ($\hat{T}_e$ or $\hat{T}_i$) to a given value at the outboard side. One of them is enough to prevent the instability because the temperatures are strongly coupled (in the model). Hence, $\hat{T}_e$ is pinned at 0.5 eV, a typical value at $r = 3$ cm, based on Gaussian fits of the TS readings in Magnum-PSI.

- Plasma inlet:
  - A fixed radial profile is chosen for the electric potential.
  - Also for the electron and ion temperatures a radial profile is set.
  - The neutral particle flux is set to zero.
  - A radial profile is set for the ion density.
  - The parallel velocity of neutrals is zero.
  - The gradient of the parallel velocity of ions is set to zero.

  For the electric potential the same inlet profile is used as done in Ref. [15] since Pilot-PSI uses the same source as Magnum-PSI. The electron temperature and electron density of the beam are determined via TS just in front of the plasma source. For the validation these profiles are used directly, but for the section where differential pumping is compared with the regular case just some typical Gaussian profiles are used: peak values $n_e = 1 \times 10^{20}\,\mathrm{m}^{-3}$, $\hat{T}_e = 3\,\mathrm{eV}$, both have a FWHM of 15 mm and the electron temperature has an offset of 0.1 eV.

  The ion temperature is assumed to equal the electron temperature, this is approximately the case 40 mm from the source in Pilot-PSI [45]. The hydrogen ion density is assumed to be the dominant ion species, and because of quasineutrality it should equal the electron density. Some simulations are conducted that use a shortened domain, meaning just the target chamber is included. Since no TS measurement data is available at the entrance of this chamber, the profiles are assumed to be unaltered in the source and heating chambers. These simulations are just used for testing some model features.

  Secondly, it is assumed that the plasma plugging is perfect, so no neutrals can leave through the inlet. The neutral particle fluxes are zero and the velocity is zero as well. Technically there is also an influx of neutral gas at the inlet, but even with a relatively high ionization degree of about 10% [29] there are still lots of neutrals coming in. However, outside of the source nozzle those neutrals spread out and most of the neutral gas that remains in the beam is ionized. As long as the model starts some distance from the nozzle $\Gamma = 0$ for neutrals is a decent approximation. Neutrals that enter via the side of the beam are already taken into account by the outboard pressure BC.

  Lastly, the parallel ion velocity at this boundary is unknown. However, the inlet is well outside of the expansion zone of the source, and "far" away from the target. Therefore axial variations are neglected, i.e. a zero axial gradient.

- Target:

- The target electric potential is floating.
- For the electron and ion temperature a sheath heat flux is applied.
- The neutral particle flux is set to zero.
- For the ion density sheath BCs are applied.
- The parallel velocity of neutrals is zero.
- The parallel velocity of ions equals the collective sound velocity.

Floating potential is defined as the potential for which the net current to the target vanishes, the current can of course still be non-zero locally. Zero flux of neutrals because there is a solid wall. Recycling of H^+ gives an additional flux of neutrals, but that is set independently by the recycling coefficients, see Section 4.1.1. It may seem that by setting the hydrogen flux, BCs for density and velocity are set. This is not the case, in the model this just sets the density BC. The momentum flux BC can be set independently of the particle flux BC.

The sheath itself is not resolved in `B2.5`, instead it is taken into account via a BC at the magnetic pre-sheath entrance. Usually the axial gradient of the ion density is chosen to be zero there[10] [23;16;25]. The parallel ion velocity is required to be greater than or equal to sound velocity at the entrance of the magnetic pre-sheath, $v_{||} \geq c_s$. This is often called the Chodura criterion, analogous to the Bohm criterion, but then for magnetized plasmas [46]. Since it is often not known by how much $v_{||}$ exceeds c_s, the marginal version is used: $v_{||} = c_s$.

In most cases the following initial conditions are used in the bulk: a homogeneous plasma with electron/ion temperature of 1.83 eV, densities of $1.25 \times 10^{19}\,\mathrm{m}^{-3}$, $4.83 \times 10^{19}\,\mathrm{m}^{-3}$, for H, H^+ respectively and a potential $\phi = 3.1\hat{T}/e = 5.673\,\mathrm{V}$. (Other values have been used as well). In exceptional cases where convergence could not be achieved, the final plasma state of a previous run with similar settings was used as initial condition. Some additional settings will be discussed in Section 4.1.1.

4.1.1 Recycling coefficients & auxiliary data

Briefly the additional settings that are required for a `B2.5` simulation are discussed, also those needed for plasmas containing lithium are already covered. When an ion flux hits the edge of the interior domain (i.e. entering the ghost cells) this is handled in `B2.5` by neutralizing the flux and returning part of it. How much is returned depends on the recycling coefficient R. The core has no recycling because this boundary has no area.

The plasma source can in theory recycle some particles, but for a fluid model this does not make sense: the bulk motion is pointing away from it. Yet, if enabled, a neutral population develops near the source, sometimes dominating the neutral densities near the target. This is totally un-physical! This much cannot be transported through the beam because it is swiftly ionized. Furthermore, it penetrates too far to be caused by inflow at the outboard side. The reason neutrals exist there is because of the ion density BCs. Once the desired ion density is overshot, the sources in the ghost cells on the inlet become negative, a flux of ions escapes the interior cells and is returned as neutrals. To counter this the recycling is disabled on the inlet, which as expected removed this population. This is not such a bad assumption since in reality most particles are moving with the beam anyway.

[10] V. Kotov describes it as: 'This "technical" boundary condition does not really affect the solution, because upwind scheme is used for this equation'. Due to the strong convection, this is purely an outflow boundary for plasma, meaning cell face values purely depend on the upstream value. The face value will equal the upstream value and hence the gradient is zero.

In steady state the recycling coefficient ate the target is 1 for hydrogen, assuming the lithium is saturated and therefore exhausts as much hydrogen as it takes in. Also without lithium the recycling coefficient is one for hydrogen. Lithium that strikes the target condenses and becomes one with the fluid, therefore the recycling rate for lithium is zero.

Finally the outboard side. This is tricky because there is no real wall there, it is the (smooth) transition from the beam to the gas. Hydrogen ions can neutralize in the outer volume and bounce back, or even bounce back from the wall into the beam. However, it does not matter which process causes the boundary value of neutral hydrogen density, this is already accounted for in the empirical pressure value. So an additional source of H due to recycling does not make sense, hence $R = 0$ for hydrogen there. For lithium a similar argument is invoked, a radial profile with a decay length of 3 cm has formed, how does not really matter, but an additional contribution by recycling should not be added on top of that. In summary, there is no recycling, except $R = 1$ on the target for hydrogen. The reason for this exception is that the value of n_H is not known on the target, but it is known that there exists a source of hydrogen due to recycling. The energy recycling coefficient is 0.3, a typical value, see Ref. [47] Sect. 1.4.2.

The anomalous[11] diffusion coefficient for ions is $D_{na} = 0.5\,\mathrm{m^2 s^{-1}}$, a value of the order of unity is a typical choice [18;48;16]. However, the exact value is less important in linear devices than in tokamaks because of the shorter connection length. I.e. less distance for particles to escape radially before they strike the target. For neutrals a pressure driven anomalous particle diffusion coefficient is used which consists of an offset C and the thermal velocity times the mean free path: $D_{pa} = C + \sqrt{\frac{\hat{T}_i}{m_i}} \frac{1}{\sigma_{CX} n_i + \sigma_{ion} n_e}$, with $C = 100\,\mathrm{m^2 s^{-1}}$, σ_{CX} the CX cross section, and σ_{ion} the ionization cross section. For hydrogen these cross sections are assumed to be a constant $5 \times 10^{-20}\,\mathrm{m^2}$ and $1.5 \times 10^{-18}\,\mathrm{m^2}$, for lithium these are 0 and $1 \times 10^{-20}\,\mathrm{m^2}$ respectively.

The ratio of specific heats is assumed to be 5/3, this is the case for an ideal mono-atomic gas. This is a fine assumption since molecules are not included in the model. Finally, the additional contribution to the energy transmission coefficient of the sheath in addition to that of the potential difference are chosen to be 2.0 for electrons and 2.5 for ions. Based on Ref. [24] for the case of zero secondary electron yield.

4.2 Differential pumping

Differential pumping is a technique to maintain a pressure difference between different parts of the vacuum system. This is accomplished by having separate chambers, connected only via a tiny aperture, where each chamber is individually pumped. The pressure will then be reduced towards to the target. The pressure values that are used in this section and later ones are given in Table 1.

Table 1: Pressures in (Pa) in each of the chambers of Magnum-PSI, used for the models that compare cases with and without differential pumping. The pressures from the most right column are typical values measured at the vessel wall in the experiments on Magnum-PSI, see Table 4. The pressures are used as a BC at the beam edge along the whole chamber. The case without differential pumping is also called the regular case.

	Without differential pumping	With differential pumping
Source chamber	1	2
Heating chamber	1	0.4
Target chamber	1	0.25

[11] The meaning of 'anomalous' differs depending on the field of research, in fusion science it is used to indicate transport that exceeds the values predicted by neoclassical theory. This is generally believed to be caused by turbulence.

The neutral hydrogen density is set using the corresponding pressure via $n = P/\hat{T}$, see Section 4.1. The value of this BC heavily impacts the neutral hydrogen density inside the beam, see Fig. 7.

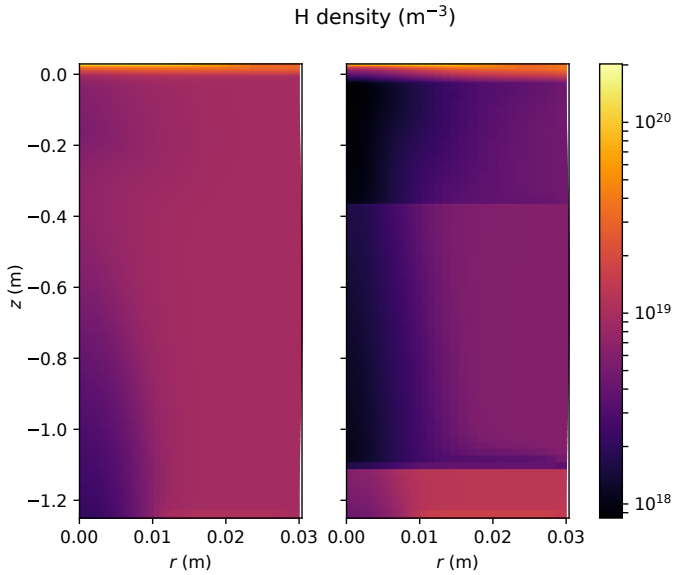

Figure 7: Neutral hydrogen density in the model of a radial cross section of the plasma beam. The left boundary is the axis of symmetry, on the right the outboard side. The source TS is at the bottom and the target is at the top. In the left panel the regular case, with just one homogeneous pressure on the outboard side. In the right panel three different pressures are applied for each chamber, see Table 1. The three chambers are already visible due to the different neutral density, from top to bottom the target, heating and source chamber.

Transitions between the chambers are quite sharp in axial direction, meaning the axial gradient length in the skimmer opening is far smaller than the average axial gradient length inside a chamber (about 60 times smaller). Apart from the region very close to the target, the neutral density is dominated by fuelling from the sides, see Appendix A.2. The axial velocity is about 10 km/s towards the target, but near the target it moves upstream with about 10 km/s. The radial velocity is only a few hundred m/s, but outflow spikes near the chamber transitions to up to a few km/s. This functions as a correction on the neutral density. Due to the jumps in BC value the sharp transitions are created. Also the temperature is affected, see next figure.

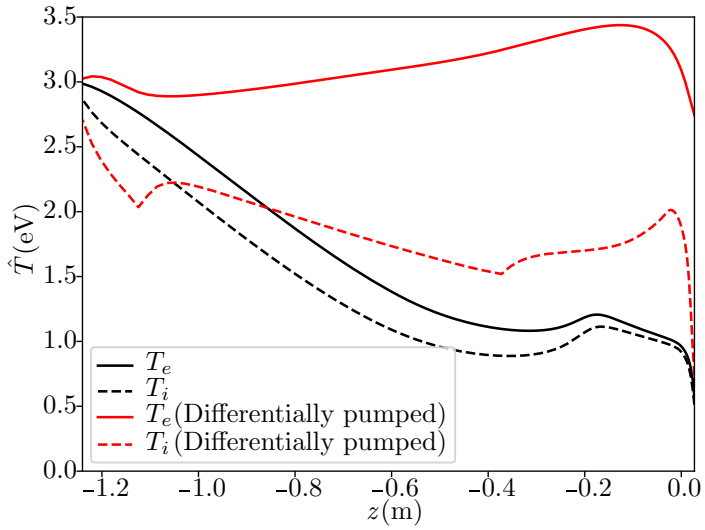

Figure 8: Axial temperature profiles for the regular and differentially pumped case [13]. In black the regular case, in red the differentially pumped case. The solid lines represent the electron temperature, the dashed ones the ion temperature. See Table 1 for the pressure settings. Due to the decreased neutral pressure less neutrals enter the domain, thus the plasma is cooled down less. A radial position of $r = 0.0003$ m is used.

There is quite a difference in temperature between the regular and differentially pumped case. The temperature can even go up with respect to the inlet, this is mostly because of Ohmic heating. Also interesting is that in the regular case the temperature rises around $z = -0.2$ m. These findings will be discussed in Section 5.2. Finally, the ion density is decreased in the differentially pumped case with respect to the regular case, see Fig. 9.

[13] Axial profiles at zero radius are not possible, `B2.5` demands a finite minimum radius, set to 10 micron in this case. Therefore in all axial profiles a small, yet finite radius is selected. Linear interpolation between the grid cells is used because the field lines are not perfectly straight, see Fig. 6.

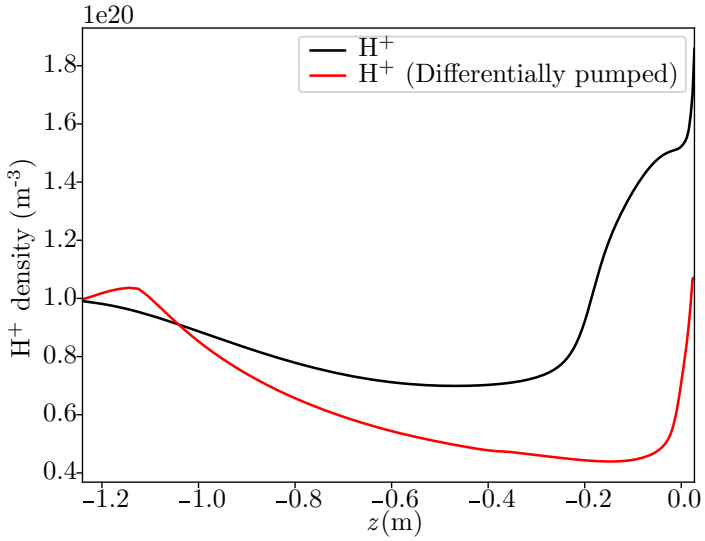

Figure 9: Axial H^+ density profiles for the regular (black) and differentially pumped case (red). See Table 1 for the pressure settings.

An axial decay in ion density is observed, however close to the target the ion density grows, this is a modelling artefact that follows from the velocity BC at the target. A detailed explanation can be found in the discussion, Section 5.2.

4.3 Experimental validation

Magnum-PSI features two TS measurement locations, see Fig. 5. To validate the predictions made by the model a comparison with downstream experimental profiles from the device is done. Several machine parameters are varied: gas flow, source current and magnetic field strength. The first two are not direct inputs of the model, but result in changes in the upstream $n_e(r), \hat{T}_e(r)$ profiles and neutral pressures. These profiles are measured with TS and used as upstream BC, the pressure is also measured at the wall and used as BC for neutral hydrogen.

This is exactly what is done, unfortunately there was a misalignment in the view port on the day when downstream measurements were conducted. This means that some optical fibres have a false sensitivity, hence the intensity is false and the downstream density is not reliable. However the temperature readings are unaffected because that is obtained from the Doppler broadening. Hence only a comparison of the downstream temperature with its predicted value is shown.

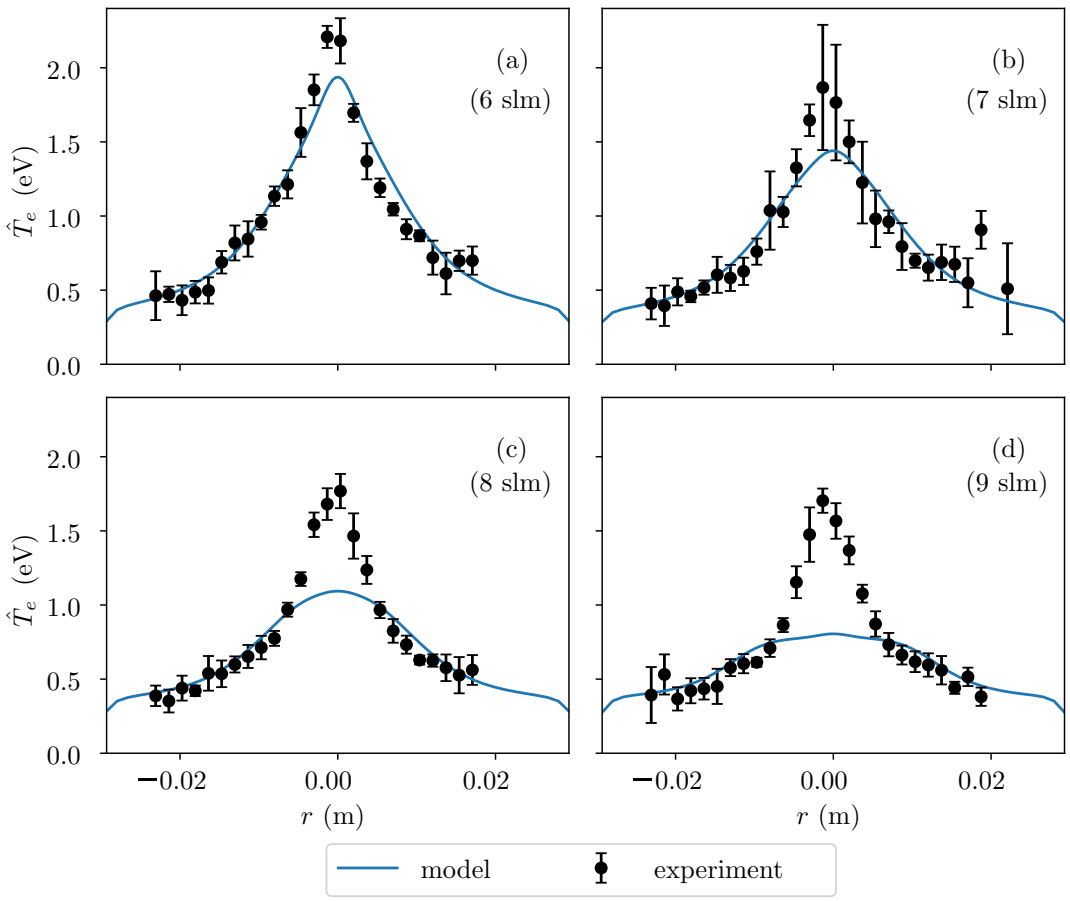

Figure 10: Electron temperature in front of the target (at $z = 0$ m) compared to model predictions. All discharges are at a magnetic field strength of 0.8 T. All four TS readings were 29.2 mm from the target, the pumping power was set to 82% of max capacity and the source current to 125 A. In all cases the target potential was floating. In discharge (a) a gas flow of 6 slm was used, 7 slm in discharge (b), 8 slm in discharge (c) and 9 slm in the last. The model agrees less at higher gas flows.

For increasing gas flow the electron temperature drops slightly, while fixing all the other parameters of the experiment: source current, magnetic field, target position, pumping rate, etc. This is the case for all tested field strengths (0.4 T, 0.8 T and 1.2 T), however the model overestimates the cooling, see Fig. 10. The same overestimation was observed at $|\mathbf{B}| = 1.2$ T. Varying the current also shows a trend, but that is less clear.

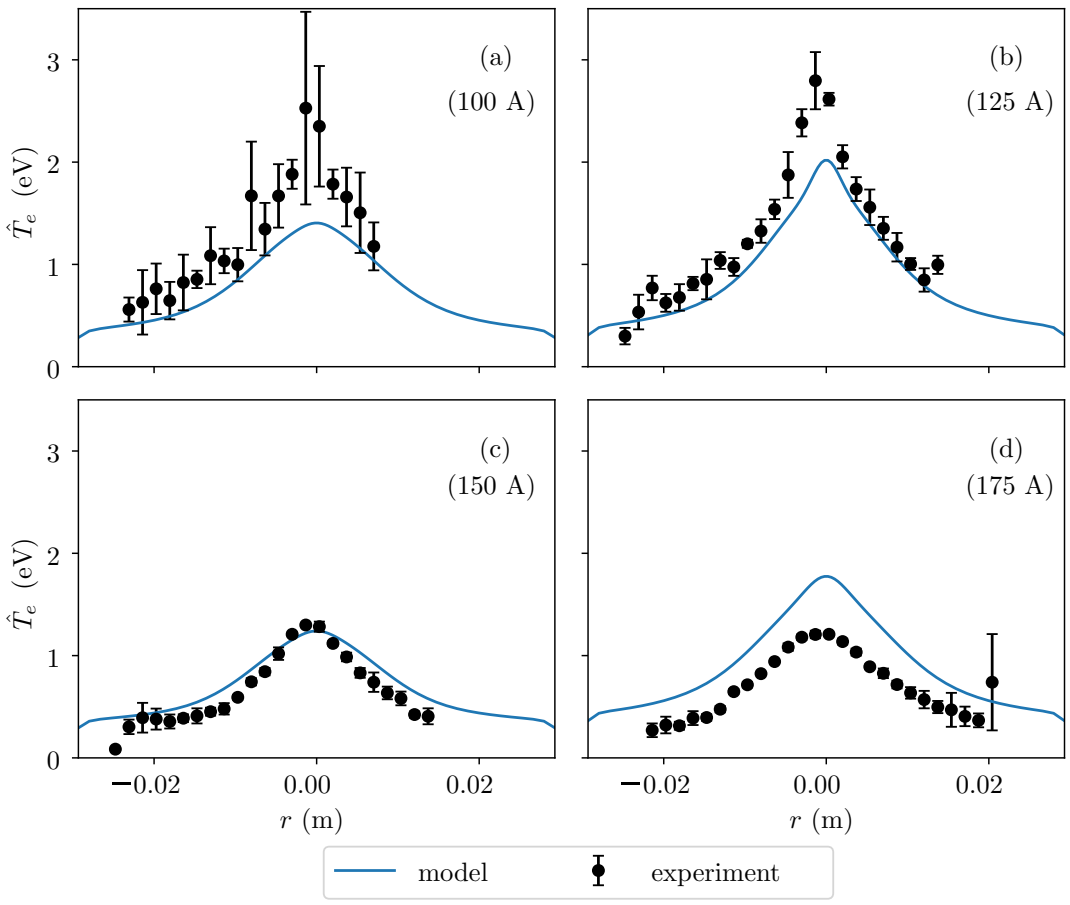

Figure 11: Electron temperature in front of the target (at $z = 0$ m) compared to model predictions. All discharges are at a magnetic field strength of 1.2 T. All four TS readings were 29.2 mm from the target, the pumping power was set to 82% of max capacity and a gas flow of 7 slm. In all cases the target potential was floating. In discharge (a) a source current of 100 A was used, 125 A in discharge (b), 150 A in discharge (c) and 175 A in the last.

Increasing the source current leads to a higher electron density, and a lower electron temperature. The transition in temperature is quite sudden, compare discharges (b) and (c) in Fig. 11. For both 0.8 T and 1.2 T the model underpredicts the temperature at low current (100 A), and overestimates the temperature at high current (175 A).

The gas flow and source current are not actually model inputs, the magnetic field, $(\hat{T}_e, n_e)$ upstream and the pressure are. The latter appears to be an important setting for the model, see Fig. 12.

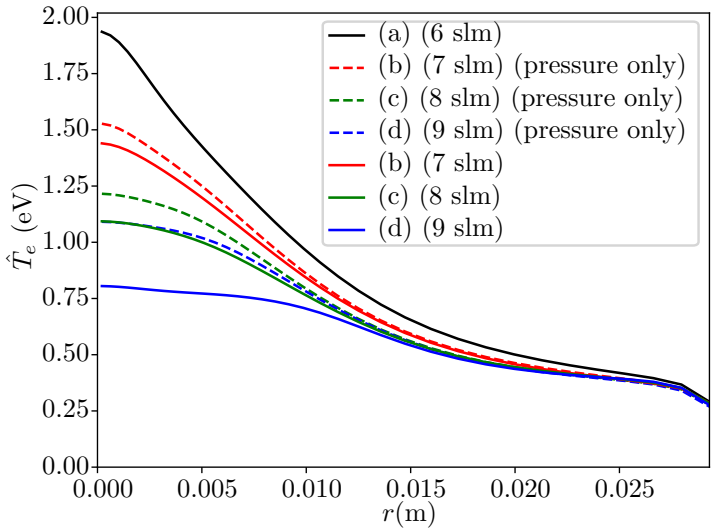

Figure 12: Radial electron temperature profile at $z = 0$ m. Models of discharges (a), (b), (c) and (d) from Fig. 10 are plotted in solid lines. In these discharges the gas flow was varied between 6 slm and 9 slm. In dashed lines the discharges (b), (c) and (d) are shown again, but now using the same upstream density and temperature profiles as discharge (a) to isolate the effect of the pressure BC on the model.

The major part of the temperature difference with respect to discharge (a) from Fig. 10 is caused by the pressure BC, this becomes clear from Fig. 12. Although varying the upstream $\hat{T}_e(r), n_e(r)$ BCs did impact the result to some extend as well.

A selection of eight discharges is show in this section, see Appendix C for the other discharges. In most of the 21 cases the model fails to reproduce the correct peak value. However the predicted values still lie within the same order of magnitude for all of the 0.8 T and 1.2 T discharges. For most cases with 0.4 T the temperature can really blow up $\hat{T}_e \sim 10$ eV. A more elaborate discussion on these results is found in Section 5.3.

5 Discussion of pure hydrogen discharge modelling results

A fluid model of the plasma beam in Magnum-PSI is made, where each heavy particle species is considered a separate fluid with its own momentum balance. For all species BCs have to be imposed on each model boundary, but there are some problems related to the experimental data. Firstly, the plasma profiles $(n_e(r), \hat{T}_e(r))$ at the plasma source contain error bars. Therefore the predictive capability of any model using these profiles has its limits. Secondly, the potential profile is assumed to be the same as in Pilot-PSI, because no measurement of this exists (yet) for Magnum-PSI. Furthermore, in this work the $\mathbf{E} \times \mathbf{B}$ and diamagnetic drifts were disabled in `B2.5` because they were found to play an insignificant role. The plasma source generates a negatively charged core[49], so there exists an azimuthal $\mathbf{E} \times \mathbf{B}$ drift. The velocity of this flow can be several km/s[15]. Also there is a pressure gradient, roughly pointing radially inwards, so also an azimuthal diamagnetic drift exists. The reason these drifts are insignificant is probably due to the direction of the drifts, namely transport in the azimuthal direction does not change the 2D results of for instance Fig. 7 because of axisymmetry. In the following sections some specific issues are discussed.

5.1 Shortcomings of the model

Predictions of the plasma temperature were compared with TS measurements for a pure hydrogen plasma. As seen in Section 4.3 there is quite a disparity. This is not unexpected because a fluid model is used for each species (H, H^+, and in some runs also Li, Li^+), even though the neutrals have a mean free path (mfp) of a few cm or more. This means the Knudsen number for neutrals can be too large ($Kn \gg 1$) to apply a fluid model, see Section 2.2. Another issue with the neutral fluid is the inherent anisotropy of the model. For ions the momentum balance is solved for the parallel component. But, transport of charged particles perpendicular to the magnetic field consists of several drift terms, plus a diffusion term that is relatively small compared to the parallel transport for magnetically confined particles. For neutrals however no such distinction between directions should be made. This leads to the very 'blocky' plot seen in Fig. 7. The neutral fluid approximation is the main limitation, and can only be solved by using a more expensive neutral model, namely a kinetic model.

Moreover, a velocity profile cannot be set upstream because then the simulation does not converge. This is circumvented by setting the velocity gradient to zero instead. Also the velocity at the magnetic pre-sheath cannot be set to the desired $v_\parallel \geq c_S$ because then the simulation diverges. As a best estimate the velocity has been set to $v_\parallel = c_S$. However, as seen in all simulations there is a significant false accumulation of ions just in front of the target because the fluid slows down to match the sound speed.

This boundary condition may also be causing the significant compression heating, leading to a bump in temperature in front of the target. Unfortunately this strongly impacts the temperature at the TS location. To make matters even worse for the validation, the temperature gradient is also quite strong at this location, see Fig. 8. More about this in Section 5.2.

Finally, neutrals that fuel the beam via the side come from a cold region, however in the current model they have the same temperature as the ions. This is taken into account to some extend because the beam edge is already relatively cold compared to the centre. This means that the injected hydrogen is also cool, but not as cold as the wall. Therefore the cooling may be underestimated.

5.2 Differential pumping

The implementation of differential pumping in the model of Magnum-PSI was described in Section 4.1, with results in Section 4.2. The temperatures in the differentially pumped case are higher

than in the regular case. The temperature can even go up with respect to the inlet, this is mostly because of Ohmic heating. In the target chamber the neutral density is the lowest, hence the line radiation losses are the least there. With the exception of just in front of the target because there a neutral cloud exists, see Fig. 7. At first hand this seems like a fine explanation of the temperature difference that differential pumping makes, but additional (hydrogen only) simulations with radiation disabled show that radiation lowers the temperature by only a few percent or less[14]. Furthermore, most line radiation originates from the inlet (H), or recombination (H^+) in the neutral cloud at the target, the bulk plasma is hardly affected. Instead, the difference in temperature between the studied cases is likely caused by the cold neutral hydrogen entering from the beam edge. All atom and ion fluids share the same temperature in the model, which is quite low at the beam edge, see for instance Fig. 10. Because neutrals move radially very effectively compared to ions and electrons, this efficiently cools down the plasma.

Notice there is a slight temperature rise around $z = -0.2$ m for the regular case in Fig. 8. At first this seems strange because the neutral pressure at the beam edge is homogeneous. It can be seen from Fig. 7 that at that location the neutral density is slightly diminished, but that is just a result of the higher temperature. The neutral density at the beam edge is not affected. Ohmic heating is rather homogeneous along the axis, however, there is also a contribution from compression heating. Heating/cooling due to compression/expansion is a known effect in thermodynamics: For an adiabatic system the increase in internal energy equals the applied work to the system. This is not readily seen from the total energy equations, Eqs. (4), first the internal and kinetic energy ought to be separated. See, Eq. (1.23), Braginskii [26] or any MHD book on two-fluid equations. It then becomes clear that $-p\nabla \cdot \mathbf{v}$ is one of the heating contributions. Normally in the simulations this term is an order of magnitude smaller than Ohmic heating, but around $z = -0.2$ m the terms become comparable due to significant slowdown of the medium. Note that Ohmic heating heats the electrons, but both the electron ($-p\nabla \cdot \mathbf{v}_e$) and ion ($-p\nabla \cdot \mathbf{v}_i$) fluids are heated by compression. See Appendix B for additional information about heating.

Finally, the ion density is plotted in Fig. 9. At the inlet the ion density is $1 \times 10^{20}\,\mathrm{m}^{-3}$, as specified by the BC. From there on out the density drops due to recombination, however just in front of the target the density starts to rise again. This is simply because of accumulation due to slowdown of the ion fluid (from about 30 km/s to 10 km/s). This slowdown is not because of collisions with neutrals, it also occurs in runs without any neutrals. It is instead caused by the the velocity required: $v_{||} = c_s$ at the magnetic pre-sheath entrance. Due to the low temperature close to the target the sound speed is small and the velocity gets artificially restricted, see Section 5.1. The condition $v_{||} \geq c_s$ unfortunately did not produce any converged runs.

5.3 Experimental validation

in Section 4.3 it was observed that the model strongly depends on the partial pressure of hydrogen at the beam edge, compared to upstream $n_e(r), \hat{T}_e(r)$ profiles. There are two problems: the pressure is not measured at the beam edge, but instead at the vessel wall. That should not be too much of a difference because the volume outside of the beam is just gas, so it is not confined to the magnetic field, hence the pressure can equilibrate. Secondly, some variance in pressure was measured in discharges using the same settings [15]. Also this should no longer be an issue after switching to a kinetic neutral model, because the boundary condition is no longer needed. Different pumping rates can be implemented by playing with the reflection rates of parts of the wall.

[14] Note here that this is only the case for these 'low' temperature plasmas, because at higher temperature radiation plays a much more significant role. Namely, the radiated power density is proportional to $\hat{T}_e^{3.9}$, see Ref. [50].

[15] In repeated experiments under the same settings the pressure was mostly found to change only within 1% in the source and heating chambers. However, there were some outliers where the pressure varied with a few percent. Secondly, the pressure in the target chamber saw regular variations of about 10%, even 20% was recorded under the same settings. So this complicates the predictive capability of the model.

Moreover, the cooling at higher gas flows (and thus neutral pressures) is overestimated in the model. This indicates that the model fails to capture some important physics. This may be caused by the outer volume that is not modelled, as discussed in the shortcomings.

Furthermore, the validation with TS measurements is done at $z = 0$ m, this is just inside the temperature bump as described in Section 5.2. Not only that, the comparison is also in a region where the temperature gradient is relatively steep, so the predicted TS profile is also very sensitive to the location of measurement.

Finally, the model predicted temperatures that were in some cases quite different from the experiment, however the predictions were of the same order of magnitude. With the exception of most of the runs at $|\mathbf{B}| = 0.4$ T. It is found that for those runs the current density went up to about $600\,\mathrm{kAm^{-2}}$, instead of the typical $80\,\mathrm{kAm^{-2}}$. This created a significant Ohmic heating contribution leading to an electron temperature of $\hat{T}_e \sim 10$ eV. Note that the ion temperature is much lower $\hat{T}_i \sim 1$ eV, which makes sense because Ohmic heating heats the electron fluid. The reason why some sets of BCs lead to and explosive current density is still unknown.

Let's revisit the following research question, "*Is it possible to model differential pumping in B2.5?*" Yes, but accuracy is limited to just the order of magnitude for most of the parameter space (0.8 T and 1.2 T discharges). The primary cause for this is probably the neutral fluid model. The research questions related to lithium are treated in Chapter 7.

6 Modelling plasmas containing lithium in Magnum-PSI

6.1 Boundary conditions for lithium

Additional BCs are required for plasma containing lithium, on top of those already mentioned in Section 4.1. No alterations have been made to those base BCs.

- Core side:
  - The Li, Li^+ particle fluxes are zero.
  - The parallel momentum fluxes for Li, Li^+ are also zero.

  This is because of axisymmetry.
- Outboard side:
  - For the Li, Li^+ densities a decay length of 3 cm is applied.
  - The parallel momentum fluxes for Li, Li^+ are set to zero.
- Plasma inlet:
  - The Li particle flux is set to zero.
  - The Li^+ density gradient is set to zero.
  - The parallel velocity of Li is zero.
  - The gradient of the parallel velocity of Li^+ is set to zero.

  The lithium ion density at the boundary is not known, in fact this is something you'd like to find (so a model output). Again the axial variations are neglected.
- Target:
  - An influx profile due to evaporation for Li is used, see Fig. 13.
  - For the Li^+ density sheath boundary conditions are applied.
  - The parallel velocity of Li is zero.
  - The parallel velocity of Li^+ is set equal to the collective sound velocity.

For the lithium neutral influx, only evaporation needs to be considered since At target temperatures exceeding 500 °C evaporation dominates sputtering, so just evaporation needs to be considered [33]. The evaporation of lithium is calculated based on the Eqs. in Sect. 2.4.1 for a realistic target temperature profile, see Fig. 13 for an example. All evaporation rates in this thesis used the same target temperature profile FWHM and offset, only the peak value was varied.

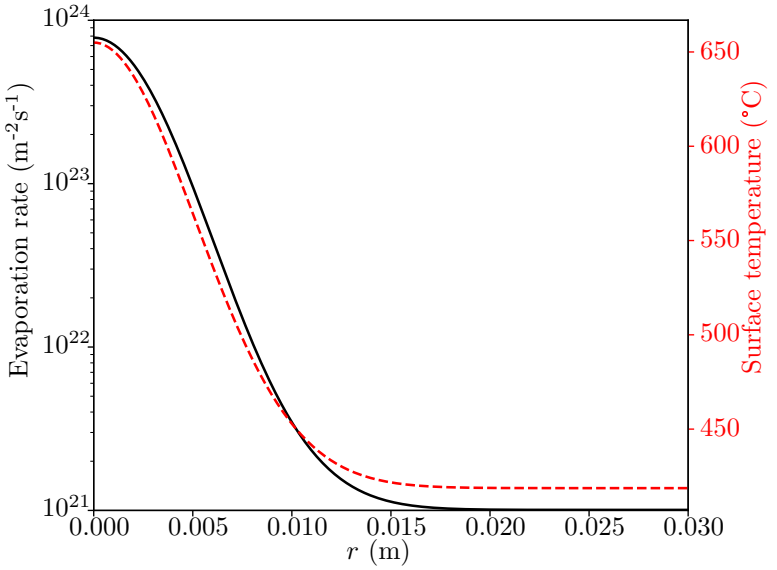

Figure 13: Example of the lithium evaporation rate at the target of Magnum-PSI as a function of radial position. A Gaussian plate temperature profile has been used with peak temperature 655 °C, with offset of 418.7 °C and FWHM of 11.97 mm, based on measurements of the target for an experiment with lithium (See Section 5.4 Ref. [22]). This profile has a peak evaporation rate of $7.79 \times 10^{23}\,\mathrm{m^{-2}s^{-1}}$. The solid line is for the evaporation rate, the dashed line represents the surface temperature.

This evaporative flux is set as a particle flux BC on the target side for neutral lithium. The initial Li, Li^+ densities are $3.1 \times 10^{20}\,\mathrm{m^{-3}}$ and $1.9 \times 10^{19}\,\mathrm{m^{-3}}$ respectively. Finally, recycling is already treated in Section 4.1.1.

6.2 Lithium distribution and comparison of the plasma with a pure hydrogen plasma

In this section the distribution of lithium over the plasma is presented, also the differential pumping is revisited. But the lithium density cannot be studied independently of the rest of the plasma, thus first the differences compared to a pure hydrogen plasma are shown. The most notable ones are seen in the electron temperature and H^+ density.

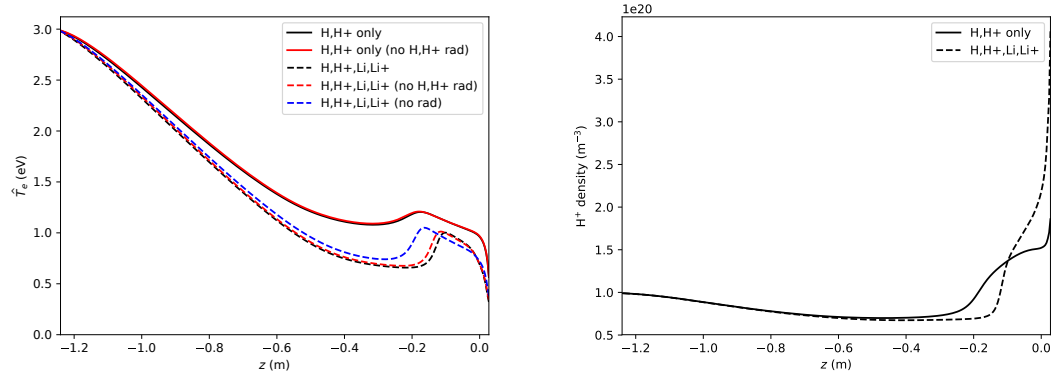

Figure 14: Axial profiles of the electron temperature (left) and H^+ density (right). In black the pure hydrogen case from Section 4.2, in red the same case but with all radiation disabled. The dashed lines represent runs with Li, Li^+ added. Two variations of the lithium simulation (black) are included, but with radiation disabled for hydrogen only (red) and all radiation disabled (blue). The evaporation rate from Fig. 13 has been used. Both cases are without differential pumping, see Table 1. These axial profiles are plotted at a radius of $r = 0.0003$ m.

The temperature shows a slight decrease compared to the pure hydrogen case. The main cooling of the plasma is caused by neutrals entering the domain. In addition to the hydrogen entering from the sides there is also lithium evaporation contributing now. Previously, in Section 5.2 it was stated that hydrogen line radiation plays only a tiny role, however lithium line radiation contributes significantly to the cooling. A similar effect is seen on the ion temperature.

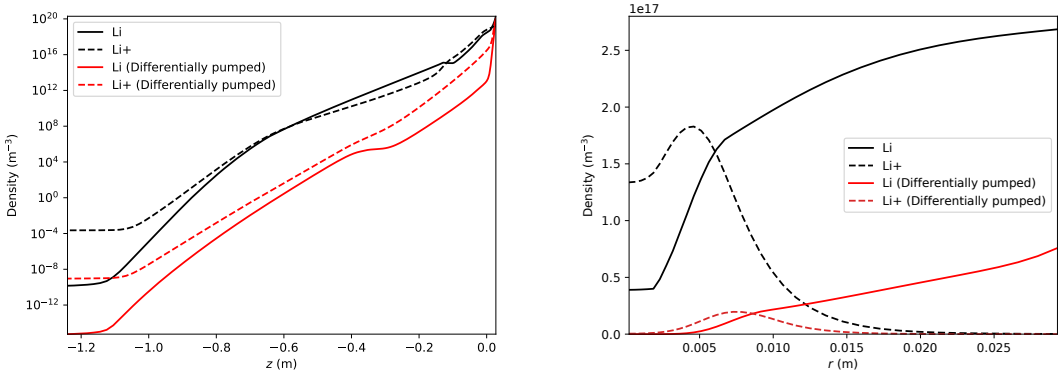

Figure 15: Axial and radial lithium density profiles. The regular case in black, the the differentially pumped case in red, see Table 1 for the pressures in each chamber. Both simulations used the Li evaporation rate from Fig. 13. The plot on the left is taken at $r = 0.0003$ m, the one on the right is captured at an axial location of $z = -0.05$ m, so about 8 cm from the target. Also note the hollow Li profile.

Note, the number density of lithium upstream is really low, practically zero for $z < -0.6$ m. As a reference, one particle per cell on this grid gives a median density of $3 \times 10^6\,\mathrm{m}^{-3}$. In the differentially pumped case the lithium neutral and lithium ion density are even lower, see the axial plot in Fig. 15. This means that either lithium leaves the beam radially more effectively, or the lithium is redeposited on the target (with recycling coefficient $R = 0$) more effectively. More about this in the discussion.

Finally, a comparison of the redeposition fraction is given in Fig. 16. This fraction is defined as the amount of lithium that returns to the target, normalized by the amount of lithium that leaves the target. This is straightforward to calculate from the model since the outflux is just the evaporation profile of Li, and the influx is simply the Li^+ particle flux.

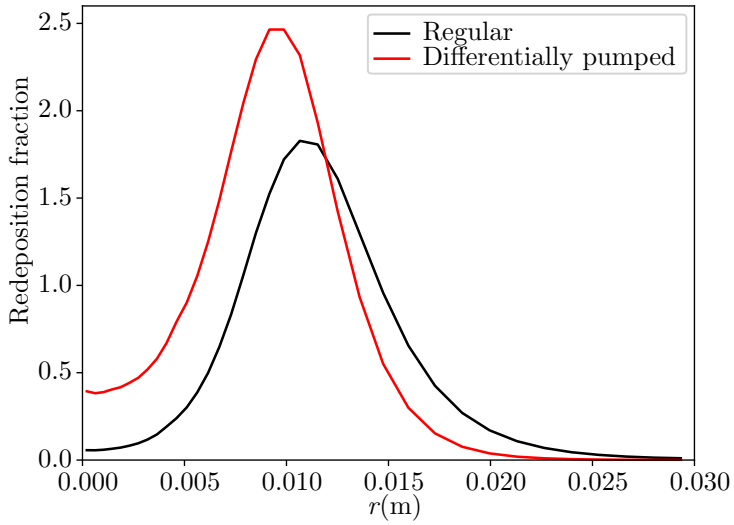

Figure 16: The redeposition fraction of lithium is plotted versus the radial position. In black the regular case, in red the differentially pumped case, see Table 1 for the pressures. The max values of $\hat{T}_e$ at the target were 0.3 eV and 0.6 eV for the regular and differentially pumped case respectively.

To clarify, the redeposition fraction can exceed 1 in places with net deposition of lithium. However, the total redeposition fraction[16] is still smaller than one, 0.23 and 0.64 for the regular and differentially pumped case respectively.

6.3 Comparison of lithium evaporation rates

In this section different Li evaporation rates are investigated, first two rates are compared in detail.

[16]Where the total redeposition fraction is defined as $\frac{\int 2\pi r \Gamma_{in} dr}{\int 2\pi r \Gamma_{out} dr}$, not $\frac{\int 2\pi r \Gamma_{in} \Gamma_{out}^{-1} dr}{\int 2\pi r dr}$.

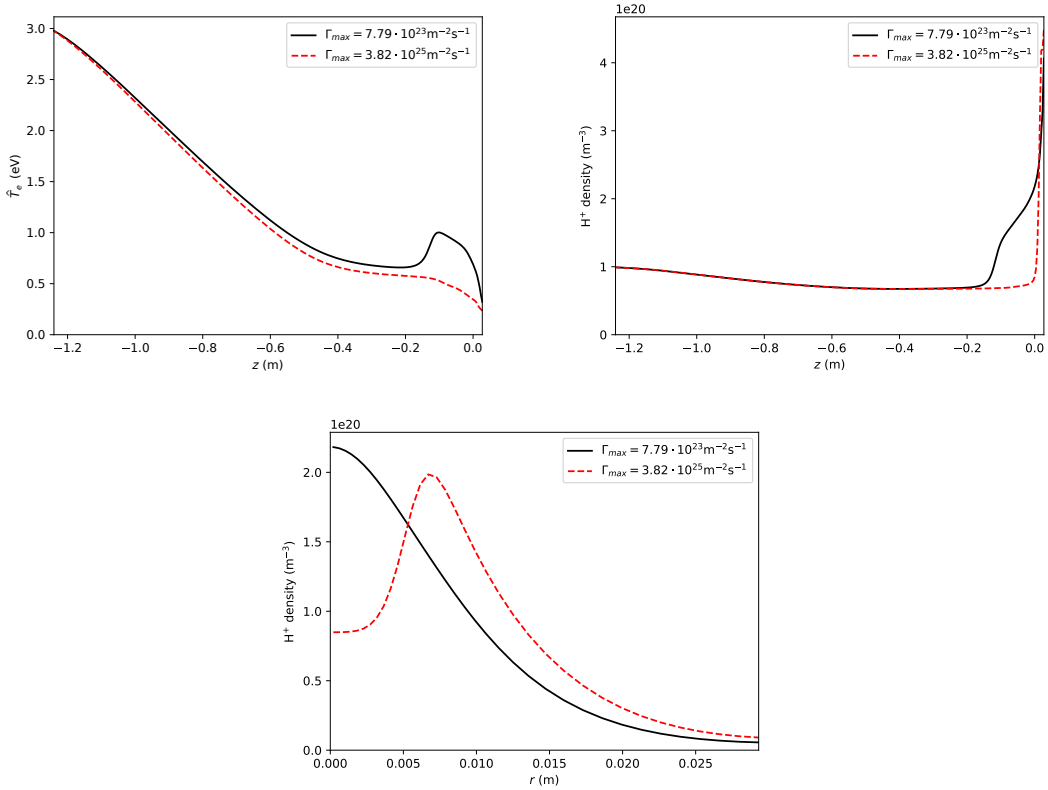

Figure 17: Axial profiles of the electron temperature (top-left), H^+ density (top-right) at $r = 0.0003$ m. In the bottom panel the radial H^+ density is shown, at $z = 0$. In black the case with a max evaporation rate of $7.79 \times 10^{23}\,\mathrm{m^{-2}s^{-1}}$, corresponding to a peak surface temperature of 655 °C. In red a run with a 49 times higher Li evaporation rate peak, namely $3.82 \times 10^{25}\,\mathrm{m^{-2}s^{-1}}$, corresponding to a surface temperature peak of 890 °C. Both cases are without differential pumping.

The ion temperature is again very similar to the electron temperature, so it is not shown. There are some interesting features: Firstly, the radial H^+ density profile close to the target is hollow for the high Li evaporation rate case. That is simply because in that case the evaporation is so strong that the plasma cools down considerably (seen in the left panel), and thus more ions recombine (and less ionization). This effect is most prominent in the centre because that is where most of the neutral lithium evaporates, hence the hollow profile. Secondly, the decrease in H^+ density is also seen in the top-right panel, but it does shoot up just before the target, that is again simply because of the velocity BC artefact.

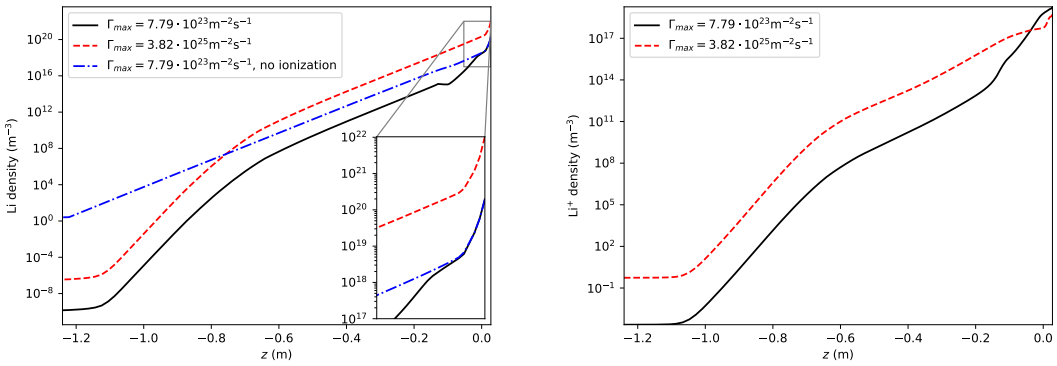

Figure 18: Axial lithium density profiles for the low vs high evaporation rate case at $r = 0.0003$ m. Also an extra variant of the low evaporation case has been included in blue from a run without Li ionization. In that run the initial Li^+ density was set to $10^{-30}\,m^{-3}$, which is effectively zero. A close-up of the first 8 cm is shown. In the first 5 cm from the target or so ionization is insignificant and the dominant loss is Li leaving the beam via the outboard side. Further upstream the main loss of Li is still outflow via the beam edge, but ionization plays a bigger role.

As expected the Li neutral density is higher if there is more evaporation, but the Li^+ density shows an interesting peculiarity. It is lower just in front of the target, for a higher evaporation rate. But this is related to the H^+ density in Fig. 17, because of the increased neutral density in front of the target a lower ion density can be maintained there. The Li neutrals now simply ionize further upstream to form Li^+ there, rather than in front of the target.

Lastly, a scan over the Li evaporation flux has been done, see Fig. 19. The same profile as in Fig. 13 has been used, except that the peak value is adjusted by powers of 7. Just as before Eq. (6) is used for the evaporation rate, again neglecting the partial pressure of lithium at the surface. These runs are a variation of the lithium case discussed in Section 6.2, so no differential pumping. Most of the interesting features have been covered in previous sections, so only the temperature and Li^+ density are shown here. The axial profile of neutral lithium density is not shown because it has almost the same shape for each evaporation rate, except that it is shifted to a higher density.

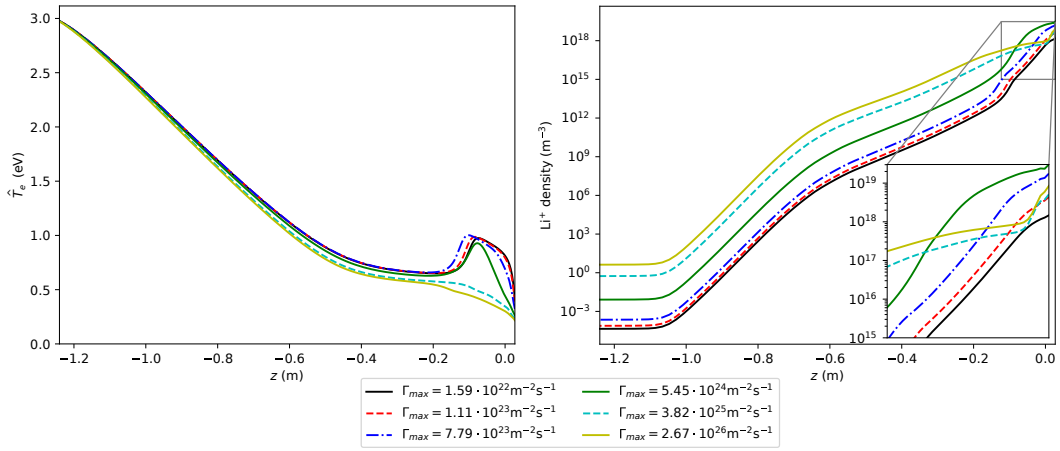

Figure 19: Axial profiles of the electron temperature (left) and Li^+ density (right) shown for various lithium fluxes. The axial profiles are interpolated at $r = 0.0003$ m. Furthermore, a zoom-in of the first 15 cm is shown. The maximum fluxes increase by a factor 7 each step, from low to high flux these peak values correspond to the following peak target temperatures: 500 °C, 570 °C, 655 °C, 759 °C, 890 °C and 1061 °C.

Interestingly, at a peak flux of $1.59 \times 10^{22}\,\mathrm{m}^{-2}\mathrm{s}^{-1}$ there is already enough lithium to show a difference compared to the pure hydrogen case (compare with Fig. 8). Furthermore, note that the lines in the right panel of Fig. 19 cross, so between $5.45 \times 10^{24}\,\mathrm{m}^{-2}\mathrm{s}^{-1}$ and $3.82 \times 10^{25}\,\mathrm{m}^{-2}\mathrm{s}^{-1}$ the lithium starts to significantly influence the plasma.

7 Discussion of model results for hydrogen plasma containing lithium

In this chapter the lithium results are discussed, and the rest of the research questions can now be answered.

7.1 Additional model limitations for lithium

"*How is the lithium that comes from a liquid target in Magnum-PSI re-distributed over the plasma* ?"
In the model most of the evaporated lithium leaves the beam radially, see Appendix A.2, however a significant fraction ionizes. In axial direction the lithium density drops rapidly to zero, see Fig. 15. However, the model has some shortcomings. Most of the shortcomings of the model have been discussed already in Section 5.1, however some additional limitations are introduced when implementing lithium, these are discussed here.

Firstly, what kind of boundary condition is to be chosen for the density of Li or Li^+ at the plasma source? The upstream density of lithium should be an output of the model, not an input. If a kinetic model is used for neutrals at least half of the issue is solved, a boundary condition for n_{Li} is then no longer required. The problem of the ions is circumvented by choosing a zero density gradient at the inlet. It is not solved though, because this boundary condition allows Li^+ to creep into the domain. This happens as follows: Li^+ is swept with the flow of the beam, so it depletes upstream, it is then refilled by the BC. So some lithium flowed in, see the upstream flux in Appendix A.2. At the moment this does not lead to significant problems because the upstream density is low anyway, so this creep is very small too. However, if in future models this flux becomes significant it may be better to set the upstream Li^+ BC to a zero flux BC.

Secondly, the model is missing some potentially important physics by omitting the volume outside of the beam. A dramatic decay in lithium density is predicted, but this is under the assumption of decay length boundary conditions for both lithium species. This means lithium can only exit through the beam edge, not enter. In reality lithium neutrals that come from the target can move upstream in the outside volume and enter the beam again, further upstream. This is not taken into account at all. Meaning the upstream lithium density may be underestimated severely. For instance, modelling of the Magnum-PSI target chamber with Eunomia standalone showed a Li density exceeding $10^{18}\,\mathrm{m}^{-3}$ outside of the beam, see Ref. [22].

Thirdly, from Appendix A.2 it becomes clear the exact value of the decay length is not so relevant for the ion density, because the outflow at the beam edge is negligible compared to the outflow at the target. However, for neutral lithium the main loss channel is outflow at the beam edge, so for Li it is important. This problem is also easily avoided when using a kinetic model for the neutrals.

Finally, it should be noted that currently the lithium CX has been neglected because `ADAS` does not have the rate coefficients for that. Only the reactions where deuterium is the donor atom are available. In the majority of the plasma this is not too bad because the lithium density is very low, see Fig. 15. However, close to the target the lithium density is significant so CX could play a role there. Also note that the `ADAS` rates are only given for a specific electron density and temperature range, typically the lower temperature bound is 0.2 eV.

7.2 Comparison with pure hydrogen model

Note that with the current BC for Li it can only exit via the beam edge, not enter. However, there is still a cooling mechanism due to lithium entering from the target at a relatively low temperature (about 0.3 eV, see Fig. 14). The overall impact of lithium on the plasma is still not that dramatic, compared to the effect of differential pumping, see Fig. 8, simply because the lithium density is

low except just in front of the target.

Since the temperature is lower near the target, compared to the hydrogen only simulation, the sound speed is lower as well. This explains the increased false accumulation of H^+ near the target in the lithium run. This accumulation artefact is discussed in Section 5.1. On top of that there is even more slowdown because of the 'slow' lithium being ionized. Once ionized it effectively exchanges momentum with H^+.

Just in front of the target the lithium neutral density is peaked in the centre because that is where the evaporation is strongest. However, further upstream the Li density profile becomes hollow as the ionization rate is higher in the beam centre. Even the Li^+ density profile becomes hollow as Li in the core is depleted, see Fig. 15.

The following question can now be answered: "*Can the lithium density be modelled with `B2.5` for Magnum-PSI?*"
Yes, but as mentioned before a more accurate (kinetic) neutral model ought to be used. Still the model captures some interesting physics such as the hollow Li profile upstream, and the transition from a regime where lithium barely impacts the plasma to one where it cools down the plasma to such a degree that the Li^+ density close to the target is lower again. More about the latter in Section 7.4.

7.3 Effect of differential pumping on lithium density

The relevant research question was: "*What is the effect of differential pumping on the lithium density in Magnum-PSI?*"
The lithium density is found to be far smaller in the differentially pumped case, see Fig. 15. After examining the sources and fluxes of lithium it is clear that this is because of the enhanced redeposition, not because of the radial Li loss rate. In fact, in the differentially pumped case even less neutral Li gets lost via the beam edge. However, due to the decreased neutral H density, the plasma is cooled down less, resulting in a higher temperature (as discussed in Section 5.2), so more lithium is ionized. The neutral lithium moves away from the target, but once ionized it is quickly speeds up to match the velocity of H^+. While for Li the main loss channel is leakage via the beam edge, and secondly ionization, for Li^+ the main loss is redeposition.

Other studies found redeposition fractions of lithium to be near unity for typical divertor plasma temperatures[36;30]. T. Abrams used a simplified model to calculate lithium density in Magnum-PSI. He describes that the redeposition fraction depends strongly on the temperature. At higher temperatures more Li ionization occurs, and Li^+ is effectively redeposited. At the beam edge the redeposition fraction is lower because Li is lost from the domain there, both of these effects are also found in this work, see Fig. 16. The fraction can even exceed 1 in regions where there is net deposition. In the model from Section 6.2 this occurs at $r \approx 1$ cm. This is caused by Li that diffuses outwards, ionizes and comes back to the target at a larger radius. Therefore the model also predicts redeposition fractions less than one in the centre. But the redeposition profiles look different from Abrams', which is not strange because in his work neutrals are assumed to leave the target in all directions with a given velocity. While in the `B2.5` model they move outwards driven by diffusion.

7.4 Effect of different evaporation fluxes

Unfortunately the validation of electron temperature cannot be done in the same way as done in Section 4.3. This is because there is a risk of damaging the TS device with lithium for measurements near the target, hence this measurement is not available. However, it is possible to validate the lithium neutral density by comparing with Li-I light intensity obtained from camera images. Such a validation was already conducted for `Eunomia` standalone. With the current setup

the validation can only be done in the first few centimetres from the target because the window is only 7.1 cm in diameter. In the examined region the lithium neutral density was found to decay exponentially as a function of the distance to the target, with a decay length of about 3-4 mm, see Ref.[22]. The results from the `B2.5` standalone simulation, see Fig. 18, have about 10 grid points in that region, enough to spatially resolve it. However, this is right where the H^+ density artefact is, so a proper comparison cannot be made.

In Section 6.3 it was found that lithium significantly starts to impact the plasma state at an evaporative Li flux between $5.45 \times 10^{24}\,\mathrm{m^{-2}s^{-1}}$ and $3.82 \times 10^{25}\,\mathrm{m^{-2}s^{-1}}$. Lithium namely cools down the plasma so less lithium is ionized right in front of the target. But of course further upstream the Li^+ density is larger for higher evaporative fluxes, see Fig. 19.

"*How does the lithium density near the plasma source depend on the evaporation rate?*"
Near the plasma source the model predicts that the lithium neutral, and lithium ion density are practically zero, even at the highest maximum evaporation rate of $2.67 \times 10^{26}\,\mathrm{m^{-2}s^{-1}}$, see Fig. 19. However, as mentioned before in Section 7.1, the transport of lithium outside of the beam is not taken into account, which can be important.

8 Conclusion

A multi-fluid model of the plasma beam in Magnum-PSI is made, spanning multiple chambers. This is used to study the transport of lithium in fusion relevant plasma. To simulate differential pumping an additional boundary condition is added to the code `B2.5`. The validation with pure hydrogen experiments shows poor agreement in general, but that is not unexpected because of the long mean free path of neutrals. Though, there is confidence in the implementation of the fluid model itself. Furthermore, the lithium density upstream is predicted to be negligibly small, but it is not clear how realistic this is because the transport of lithium outside of the beam is omitted. The model also shows the lithium density is significantly reduced in a differentially pumped case. Finally, coupling with a kinetic neutral model is required, this will also tackle some of the current model's artefacts.

8.1 Outlook

In the future there is room for improvement. As already indicated before, coupling with the kinetic code `Eunomia` is a priority. The experimental validation should be revisited afterwards.

Addition of a kinetic model can also take into account the rich molecular chemistry inside a plasma. Molecules can play an important role in the SOL [51;15;25]. Including for instance lithium hydrides is worth exploring. However, molecular ions cannot be tracked in space. `Eirene` and `Eunomia` can take them into account, but only as an additional reaction channel, meaning they are used in a reaction instantly. `B2.5` also cannot model molecular ions, only atomic species (at the moment of writing). However, even if it could, there is currently no molecular data in `ADAS` or stra[17]. But that is being worked on, see adas-fusion.eu.

Furthermore, for now the neutral flux from the plasma source has been neglected. Typically the ionization degree is 10% at the source nozzle, however outside the neutrals quickly fly off and the beam maintains an even higher ionization degree. Remember, the model's upstream boundary is not at the nozzle, but at the source TS location. However, if the outer volume is also to be modelled the neutral particle flux at the source should be included. Otherwise there is no source of hydrogen neutrals except from recombination, also there would be no differentiating between cases with different gas flow.

In the lithium models the evaporation flux is assumed to be a given, fixed quantity. However, in a steady state experiment the target temperature is a given, fixed quantity. So when validating the lithium model results it becomes important to correct for the partial pressure of lithium (Li and Li^+), see Eq. (6). This pressure can be quite significant, e.g. for the run with a max evaporation rate of $7.79 \times 10^{23}\,\mathrm{m^{-2}s^{-1}}$ the vapour pressure went up to 24 Pa and the partial pressure of lithium went up to 11 Pa. This needs to be done in the code itself (`B2.5` or `Eunomia`) because feedback from the system's state is required. There is a built-in model for thermal evaporation in `B2.5`, see `b2stbr_therm_evap`, but that also does not (yet) compensate for the partial pressure.

The recycle rate was found to be of great influence on the ion and neutral density. Lithium coatings of a few micron, exposed to deuterium plasma are saturated with deuterium within seconds [40]. So currently a recycling rate of 1 for hydrogen has been used at the target, but other values are still worth exploring. For instance for flowing targets such as the LiMIT (liquid-metal infused trenches) design the surface gets refreshed continuously and the recycling rate could be closer to 0.

Furthermore, the target potential was set to be floating in the model, but a target bias can significantly effect the current profile and thus the temperature profile via Ohmic heating, see Appendix B. Therefore it would be interesting to investigate different target biases, but also

[17] The Amjuel database has molecular data, but no lithium hydrides.

different upstream potential profiles. Last but not least, it would be of interest to apply a coupled fluid-kinetic model to a real tokamak vapour box geometry.

9 Bibliography

[1] I. P. E. G. on Divertor, I. P. E. G. on Divertor Modelling, Database, and I. P. B. Editors, "Chapter 4: Power and particle control," *Nuclear Fusion*, vol. 39, no. 12, p. 2391, 1999.

[2] J. G. Lambert, C. A. Hall, S. Balogh, A. Gupta, and M. Arnold, "Energy, eroi and quality of life," *Energy Policy*, vol. 64, pp. 153 – 167, 2014.

[3] "U.s. energy information administration - eia - independent statistics and analysis," May 2016. `https://www.eia.gov/outlooks/ieo/world.php`.

[4] The MIT Joint Program on the Science and Policy of Global Change, "2014 energy and climate outlook," 2014.

[5] "Renewable energy & efficiency partnership (august 2004), visited 22 february 2018." Available at `https://www.reeep.org/sites/default/files/Glossary%20of%20Terms%20in%20Sustainable%20Energy%20Regulation.pdf`.

[6] J. Ongena and G. Van Oost, "Energy for future centuries: Will fusion be an inexaustible, safe and clean energy source?," *Transactions of fusion science and technology*, vol. 45, pp. 3–14, 2004.

[7] P. Rebut, D. Boucher, D. Gambier, B. Keen, and M. Watkins, "The key to iter: the divertor and the first wall," tech. rep., 1993.

[8] G. Janeschitz, K. Borrass, G. Federici, Y. Igitkhanov, A. Kukushkin, H. Pacher, G. Pacher, and M. Sugihara, "The iter divertor concept," *Journal of Nuclear Materials*, vol. 220-222, pp. 73 – 88, 1995. Plasma-Surface Interactions in Controlled Fusion Devices.

[9] A. Kukushkin, H. Pacher, G. Janeschitz, A. Loarte, D. Coster, G. Matthews, D. Reiter, R. Schneider, and V. Zhogolev, "Basic divertor operation in iter-feat," *Nuclear fusion*, vol. 42, no. 2, p. 187, 2002.

[10] M. Narula, M. Abdou, A. Ying, T. Sketchley, and J. Burris, "Study of liquid metal film flow characteristics under fusion relevant magnetic field conditions," in *Fusion Engineering, 2003. 20th IEEE/NPSS Symposium on*, pp. 2–5, IEEE, 2003.

[11] PPPL, "Ltx fact sheet - princeton plasma physics laboratory," 2011.

[12] M. Ono, M. a. Jaworski, R. Kaita, H. W. Kugel, J.-W. Ahn, J. P. Allain, M. G. Bell, R. E. Bell, D. J. Clayton, J. M. Canik, S. Ding, S. P. Gerhardt, T. K. Gray, W. Guttenfelder, Y. Hirooka, J. Kallman, S. Kaye, D. Kumar, B. P. LeBlanc, R. Maingi, D. K. Mansfield, a. G. McLean, J. Menard, D. Mueller, R. E. Nygren, S. F. Paul, M. Podesta, R. Raman, Y. Ren, S. a. Sabbagh, F. Scotti, C. H. Skinner, V. Soukhanovskii, V. Surla, C. N. Taylor, J. Timberlake, and L. E. Zakharov, "Recent progress in the NSTX/NSTX-U lithium programme and prospects for reactor-relevant liquid-lithium based divertor development," *Nuclear Fusion*, vol. 53, no. 11, p. 113030, 2013.

[13] R. J. Goldston, R. Myers, and J. Schwartz, "The lithium vapor box divertor," *Physica Scripta*, vol. 2016, no. T167, p. 014017, 2016.

[14] P. Fiflis, T. Morgan, S. Brons, G. Van Eden, M. Van Den Berg, W. Xu, D. Curreli, and D. Ruzic, "Performance of the lithium metal infused trenches in the magnum PSI linear plasma simulator," *Nuclear Fusion*, vol. 55, no. 11, p. 113004, 2015.

[15] R. Wieggers, *B2.5-Eunomia simulations of Pilot-PSI*. PhD thesis, 2012.

[16] H. Kastelewicz and G. Fussmann, "Plasma modelling for the psi linear plasma device," *Contributions to Plasma Physics*, vol. 44, no. 4, pp. 352–360, 2004.

[17] L. W. Owen, J. F. Caneses, J. Canik, J. D. Lore, C. Corr, B. Blackwell, X. Bonnin, and J. Rapp, "B2.5-eirene modeling of radial transport in the magpie linear plasma device," *Plasma Sources Science and Technology*, vol. 26, no. 5, p. 055005, 2017.

[18] M. Baeva, W. J. Goedheer, N. J. Lopes Cardozo, and D. Reiter, "B2-EIRENE simulation of plasma and neutrals in MAGNUM-PSI," *Journal of Nuclear Materials*, vol. 363-365, no. 1-3, pp. 330–334, 2007.

[19] J. Rapp, L. W. Owen, X. Bonnin, J. F. Caneses, J. M. Canik, C. Corr, and J. D. Lore, "Transport simulations of linear plasma generators with the B2.5-Eirene and EMC3-Eirene codes," *Journal of Nuclear Materials*, vol. 463, pp. 510–514, 2015.

[20] K. Ješko, Y. Marandet, H. Bufferand, J. Gunn, H. van der Meiden, and G. Ciraolo, "Soledge2d-eirene simulations of the pilot-psi linear plasma device compared to experimental data," *Contributions to Plasma Physics*, pp. 1–7, 2018.

[21] K. Beks-Peerenboom, *Modeling of magnetized expanding plasmas*. PhD thesis, 2012.

[22] R. Chandra, "Simulation of neutral lithium atoms in Magnum-PSI using Eunomia." 2017.

[23] D. Coster, O.Wenisch, K. Kukushkin, A. Kukushkin, A. Chin, D. Stotler, M. Stanojevic, X. Bonnin, S. Voskoboynikov, *et al.*, "SOLPS 5.0 manual 2013 draft." 2013.

[24] M. Baelmans, *Code improvements and applications of a two-dimensional edge plasma model for toroidal devices*. PhD thesis, 1994.

[25] V. Kotov, D. Reiter, and A. S. Kukushkin, *Numerical study of the ITER divertor plasma with the B2-EIRENE code package*. PhD thesis, 2007.

[26] S. I. Braginskii, *Transport processes in a plasma*, vol. 1. 1965.

[27] R. Fitzpatrick, *Plasma Physics: An Introduction*. Taylor & Francis, 2014.

[28] I. Hutchinson, "Lecture notes: Introduction to plasma physics." `http://silas.psfc.mit.edu/introplasma/`, 2001.

[29] H. Van Eck, W. Koppers, G. van Rooij, W. Goedheer, R. Engeln, D. Schram, N. L. Cardozo, and A. Kleyn, "Modeling and experiments on differential pumping in linear plasma generators operating at high gas flows," *Journal of applied physics*, vol. 105, no. 6, p. 063307, 2009.

[30] T. W. Abrams, *E Rosion and Re - Deposition of Lithium and Boron Coatings Under High - Flux Plasma Bombardment*. PhD thesis, 2015.

[31] D. Reiter, "Amjuel manual," Nov 2017. `http://www.eirene.de/amjuel.pdf`.

[32] T. Morgan, P. Rindt, G. van Eden, V. Kvon, M. Jaworksi, and N. L. Cardozo, "Liquid metals as a divertor plasma-facing material explored using the pilot-psi and magnum-psi linear devices," *Plasma Physics and Controlled Fusion*, vol. 60, no. 1, p. 014025, 2017.

[33] R. Kaita, P. Efthimion, D. Hoffman, B. Jones, H. Kugel, R. Majeski, T. Munsat, S. Raftopoulos, G. Taylor, J. Timberlake, V. Soukhanovskii, D. Stutman, M. Iovea, M. Finkenthal, R. Doerner, S. Luckhardt, R. Maingi, and R. Causey, "Diagnostics for liquid lithium experiments in CDX-U," *Review of Scientific Instruments*, vol. 72, no. 1 II, pp. 915–918, 2001.

[34] R. E. Honig, *Vapor pressure data for the solid and liquid elements*, vol. 30. 1969.

[35] D. Coster, O.Wenisch, K. Kukushkin, A. Kukushkin, A. Chin, D. Stotler, M. Stanojevic, X. Bonnin, S. Voskoboynikov, *et al.*, "Solps-iter manual 2016 draft." 2016.

[36] J. Brooks, T. Rognlien, D. Ruzic, and J. Allain, "Erosion/redeposition analysis of lithium-based liquid surface divertors," *Journal of Nuclear Materials*, vol. 290, pp. 185 – 190, 2001. 14th Int. Conf. on Plasma-Surface Interactions in Controlled Fusion Devices.

[37] E. L. Vold, F. Najmabadi, and R. W. Conn, "Fluid model equations for the tokamak plasma edge," *Physics of Fluids B: Plasma Physics*, vol. 3, no. 11, pp. 3132–3152, 1991.

[38] R. Chodura, "Plasma flow in the sheath and the presheath of a scrape-off layer," in *Physics of plasma-wall interactions in controlled fusion*, pp. 99–134, Springer, 1986.

[39] P. Stangeby, *The Plasma Boundary of Magnetic Fusion Devices*. Series in Plasma Physics and Fluid Dynamics, Taylor & Francis, 2000.

[40] T. Abrams, M. Jaworski, M. Chen, E. Carter, R. Kaita, D. Stotler, G. D. Temmerman, T. Morgan, M. van den Berg, and H. van der Meiden, "Suppressed gross erosion of high-temperature lithium via rapid deuterium implantation," *Nuclear Fusion*, vol. 56, no. 1, p. 016022, 2016.

[41] G. Kroesen, D. Schram, and J. De Haas, "Description of a flowing cascade arc plasma," *Plasma Chemistry and Plasma Processing*, vol. 10, no. 4, pp. 531–551, 1990.

[42] H. J. N. van Eck, *The linear plasma generator Magnum-PSI*. Technische Universiteit Eindhoven, 2013.

[43] M. Furubayashi, K. Hoshino, M. Toma, A. Hatayama, D. Coster, R. Schneider, X. Bonnin, H. Kawashima, N. Asakura, and Y. Suzuki, "Comparison of kinetic and fluid neutral models for attached and detached state," *Journal of Nuclear Materials*, vol. 390, pp. 295–298, 2009.

[44] A. Hatayama, H. Segawa, R. Schneider, D. Coster, N. Hayashi, S. Sakurai, N. Asakura, and M. Ogasawara, "High mach flow associated with x point marfe and plasma detachment," *Nuclear fusion*, vol. 40, no. 12, p. 2009, 2000.

[45] H. J. Van der Meiden, J. W. Vernimmen, K. Bystrov, K. Jesko, M. Y. Kantor, G. De Temmerman, and T. W. Morgan, "Collective Thomson scattering system for determination of ion properties in a high flux plasma beam," *Applied Physics Letters*, vol. 109, no. 26, pp. 1–12, 2016.

[46] P. Stangeby, "The bohm–chodura plasma sheath criterion," *Physics of plasmas*, vol. 2, no. 3, pp. 702–706, 1995.

[47] E. M. Granstedt, *The Low-Recycling Lithium Boundary and Implications for Plasma Transport*. PhD thesis, Princeton University, 2013.

[48] B. Braams, "Radiative divertor modelling for iter and tpx," *Contributions to Plasma Physics*, vol. 36, no. 2-3, pp. 276–281, 1996.

[49] D. Borodin, A. Kirschner, D. Nishijima, R. Doerner, J. Westerhout, G. J. van Rooij, J. Rapp, A. Kreter, R. Ding, A. Galonska, and V. Philipps, "Modelling of impurity transport in the linear plasma devices PISCES-B and Pilot-PSI using the monte-carlo code ERO," *Contributions to Plasma Physics*, vol. 50, no. 3-5, pp. 432–438, 2010.

[50] W. Vijvers, *A high-flux cascaded arc hydrogen plasma source*. PhD thesis, Technische Universiteit Eindhoven, 2011.

[51] K. Ješko, H. van der Meiden, J. Gunn, J. Vernimmen, and G. D. Temmerman, "Plasma pressure and particle loss studies in the pilot-psi high flux linear plasma generator," *Nuclear Materials and Energy*, vol. 12, pp. 1088 – 1093, 2017. Proceedings of the 22nd International Conference on Plasma Surface Interactions 2016, 22nd PSI.

A Internal validation

A.1 Grid resolution

A run with hydrogen and lithium (target chamber only) has been executed on several different grid sizes ranging from 8x8 to 128x32[18].

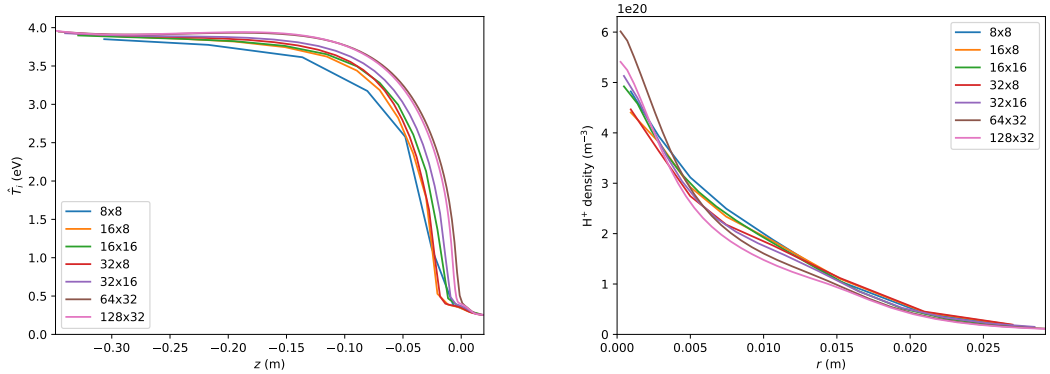

Figure 20: Example of different results on various resolutions. The ion temperature is shown on the left, the H^+ density on the right. A magnetic field strength of 2.5 T was used. Some discrepancies exist near the target, mostly where large gradients in density are present. In principle the quantities of interest are only known on the grid points, so to compare them they are interpolated (linearly) on some radial or axial location. Since there are no grid points exactly on axis the comparison is made slightly off centre, $r = 0.001$ m in this case. The radial plot is at $z = 0$ m.

Simulation results look very similar, even on the coarse 8x8 grid! This means lower resolution runs are excellent for exploratory work. At higher resolutions the diminishing returns are visible, see Fig. 21. There are many ways to characterise the differences, plotting the extremes is chosen because these are very sensitive to the refinement of the grid.

[18]The max resolution of `B2.5` is 128x36.

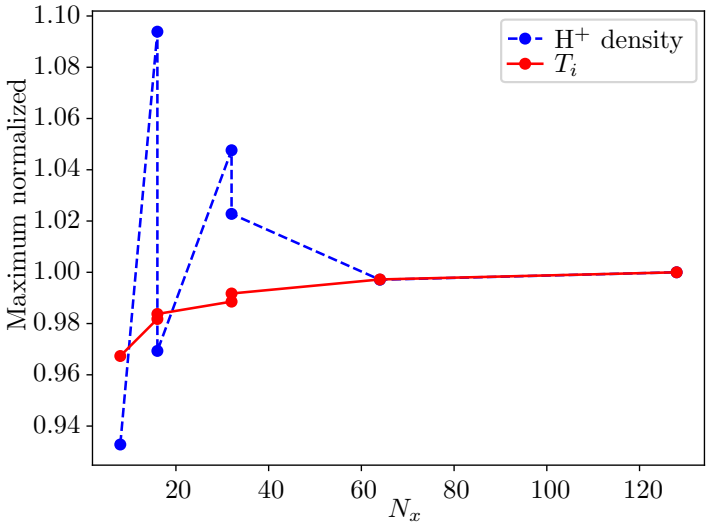

Figure 21: Maximum hydrogen ion density and ion temperature, normalized to the value for the highest resolution grid. Plotted versus the parallel resolution N_x. For $N_x = 16, 32$ two simulations are conducted each, for $N_y = 8, 16$. A visible improvement is seen for higher radial resolution as well.

All tested grid sizes show the same qualitative behaviour, but some quantitative differences in regions with strong gradients. The optimal resolution is found to be 64x32, since not much is gained by having more points than that, at least for the short geometry that is. The full device is about 3.5 times longer, so the maximum resolution 128x36 is used for that geometry.

A.2 Particle conservation

In steady state Eq. (1a) reduces to: $\nabla \cdot \mathbf{\Gamma}_i = S_{n_i}$. Integrating over a (cell) volume and using the divergence theorem yields:

$$\oint_A \mathbf{\Gamma}_i \cdot d\mathbf{A} = \int_v S_{n_i} dv \tag{8}$$

This makes sense, if particles cannot accumulate then what flows in must disappear due to a sink term. Let's examine the global conservation (so for the whole domain) of particle density for the simulation described in Chapter 6, with peak Li evaporation rate of $7.79 \times 10^{23}\,\mathrm{m^{-2}s^{-1}}$ and without differential pumping.

Table 2: The area integrated fluxes and volume integrated sources (particles/s). Normally positive flux means particles flow in the direction of increasing poloidal or radial index, to avoid confusion here positive flux means there is a net flux into the domain.

species→ boundary↓	H	H$^+$	Li	Li$^+$
W (target)	4.75468e+20	-4.75469e+20	3.23867e+19	-7.33282e+18
E (inlet)	1.49075e+14	4.92660e+20	7.64646e-08	1.87798e-04
N (outboard)	-4.88356e+20	-4.30162e+18	-2.50537e+19	-2.78264e+14
S (axis)	6.25473e+11	1.90891e+12	4.81197e+11	-2.72240e+10
Total	-1.28876e+19	1.28903e+19	7.33308e+18	-7.33310e+18
Source	1.28903e+19	-1.28903e+19	-7.33310e+18	7.33310e+18

There are some interesting things that can be learned from Table 2: A zero flux BC has been used on the west boundary for the neutral hydrogen density, yet there is a flux. That is because the flow of H^+ that intersects the target is recycled completely (in this model) and injected into the domain. Recycling is independent on the BC. There is a slight discrepancy in fluxes, this indicates that the residual is not so small yet that the machine precision becomes the limiting factor. Secondly, the flux on the south boundary is negligibly small. In theory it should be exactly zero because the axis has zero area, however in the model this is not possible because each boundary requires some surface area. Hence there is a small, yet finite flux. Thirdly, as expected the sources cancel out the total fluxes. Note that also the sum over the sources of the same atomic type cancels out, this is logical because H can only transform into H^+ and visa versa (same story for lithium). Fourthly, the model was found to be very insensitive to the value of the decay length (at least for ions), this is now explained because most of the fluid is already lost to the target before it can leak out radially. Finally: H mainly comes from the target and it is then lost at the beam edge. The slight mismatch is compensated for by recombination of H^+. H^+ enters the domain at the inlet and 'leaves' at the target. Li comes from the target, at is mainly lost via the beam edge. The excess is ionized and then deposited back on the target.

The main source of neutral hydrogen is recycling at the target, this dominates the density in front of it. However, this does not mean that recycling also determines how hydrogen neutrals are distributed in the bulk. Let's examine another control volume, instead of the whole domain:

Table 3: The area integrated fluxes and volume integrated sources (particles/s). The volume of integration ranges from source up to about 15 cm from the target. (To be precise, from $z = -1.25$ m to $z = -0.12252187224808$ m, over the full radial range).

species→ boundary↓	H	H^+	Li	Li^+
W	-9.15594e+19	-4.89509e+20	8.84162e+15	-2.33160e+15
E(inlet)	1.49075e+14	4.92660e+20	7.64646e-08	1.87798e-04
N(outboard)	9.02538e+19	-1.84374e+18	-6.50982e+15	-1.99489e+11
S(axis)	-1.57193e+10	1.45689e+12	1.95650e+04	-7.12372e+06
Total	-1.30544e+18	1.30809e+18	2.33180e+15	-2.33180e+15
Source	1.30809e+18	-1.30809e+18	-2.33180e+15	2.33180e+15

Also in this control volume the sources cancel out the total fluxes, as they should. But there are some differences with Table 2, the west side H flux is now pointed towards the target, H is replenished via the beam edge. This means that most of the recycled hydrogen just lingers near the target and then leaves via the beam edge. For lithium most of the upstream flux at the west has died down, so also most lithium stays close to the target, and then gets lost at the beam edge.

B Heating of the plasma

Internal energy can be transported in various ways, see Eq. (4a). But net heating *inside* the plasma happens only via viscous heating (due to $\mathbf{\Pi}$), heating due to electron-atom friction (a.k.a. Joule or Ohmic heating, due to $\mathbf{R}$), compression[19], or by an energy source S. The most important heat source inside the plasma of Magnum-PSI is Ohmic heating, followed by compression heating. The most important loss channel is radiation, followed by ionization energy losses. *Inside*, so excluding the important energy flux from the plasma source, the energy dump at the target and the cooling from neutral hydrogen entering the beam.

[19] In compression kinetic energy gets converted into internal energy, thus increasing the temperature.

To give an idea about the influence of some of the terms the max value on axis is given for the pure hydrogen run in Section 4.2 without differential pumping: Ohmic heating accounts for about $8 \times 10^6\,\mathrm{Wm}^{-3}$, pretty homogeneous in axial direction. Compression heating results in about $2 \times 10^6\,\mathrm{Wm}^{-3}$, peaked at $z = -0.2$, only $-p\nabla \cdot \mathbf{v}_e$ counted but the ions experience a comparable heating. Bremsstrahlung mostly bunched up near the inlet and target, and accounts for about $500\,\mathrm{Wm}^{-3}$, so totally negligible. Line radiation is split into two contributions: that of neutral hydrogen, and that of H^+ that recombines into an excited state and immediately decays. The first gives about $4 \times 10^5\,\mathrm{Wm}^{-3}$ near the inlet, recombinative line radiation about $6 \times 10^5\,\mathrm{Wm}^{-3}$. This second contribution is very localized near the target. Finally, energy losses due to ionization account for another $1 \times 10^5\,\mathrm{Wm}^{-3}$, mostly near the inlet.

The power varies a lot from run to run, but the most important contribution is the Ohmic heating. This will be discussed further below. Current runs from the anode, located a few millimetres from the core, to the cathode in the core. However, it cannot do this directly, because charged particles are confined to the magnetic field. Although some radial current exists due to diffusion, most current runs to the target first, then travels radially inwards inside the target, and then back to the cathode through the plasma core. Ohmic heating scales with current density squared, $dP/dV = \eta j^2$. The area through which the current from the anode runs is larger than that through which the returning current runs, thus most of the heating happens in the core. Modelling with floating target potential indeed predict this. However, when a target bias is applied (e.g. $-50\,\mathrm{V}$) the departing current is strengthened, while the returning current is weakened. See Fig. 22.

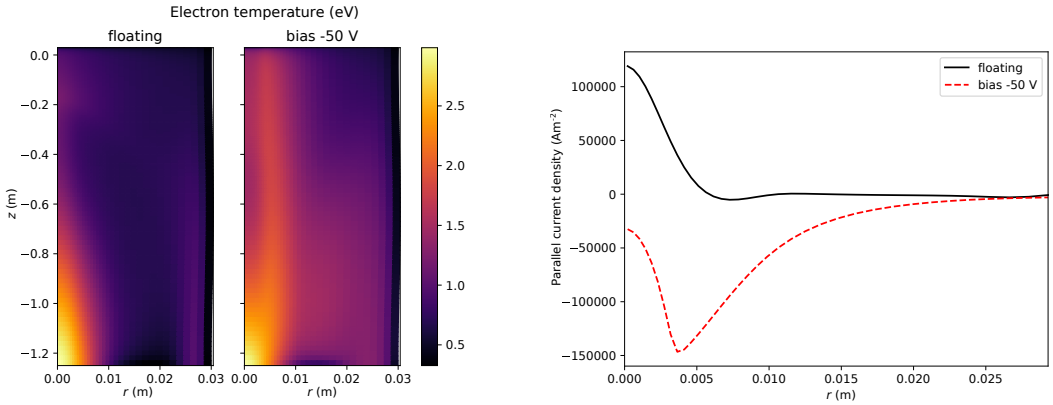

Figure 22: A run with species H and H^+, comparing floating and biased targets. This can drastically influence the temperature. Density and velocity profiles are affected, but less severe. In the right panel the parallel current density is plotted at the TS location, here negative means the current runs towards the target. Radial current is also calculated by the model, but that is completely negligible compared to the parallel current, so only the latter is shown.

Modelling shows that downstream the peak temperature is located off centre. In some cases the Ohmic heating is so strong that the maximum exceeds the inlet value! Note, R. Wieggers gives a nice explanation about current in his thesis [15].

C Experiment list

The discharges used in the validation are listed below.

Table 4: Experimental measurements conducted in Magnum-PSI on 21 and 22 December, 2017. All TS readings were 29.2 mm from the target, the pumping power was set to 82% of max capacity and the target potential was floating. The discharges are presented in the same order as they were conducted.

TS# (upstream)	TS# (downstream)	Source current (A)	gas flow (slm)	Magnetic field strength (T)
12524	12579	125	7	0.8
12525	12580	125	6	0.8
12526	12581	125	8	0.8
12527	12582	125	9	0.8
12528	12583	100	7	0.8
12529	12584	150	7	0.8
12530	12585	175	7	0.8
12540	12605	125	7	1.2
12541	12606	125	6	1.2
12542	12607	125	8	1.2
12543	12608	125	9	1.2
12544	12609	100	7	1.2
12545	12610	150	7	1.2
12546	12611	175	7	1.2
12547	12571	125	7	0.4
12548	12572	125	6	0.4
12549	12574	125	8	0.4
12550	12575	125	9	0.4
12551	12576	100	7	0.4
12552	12577	150	7	0.4
12553	12578	175	7	0.4

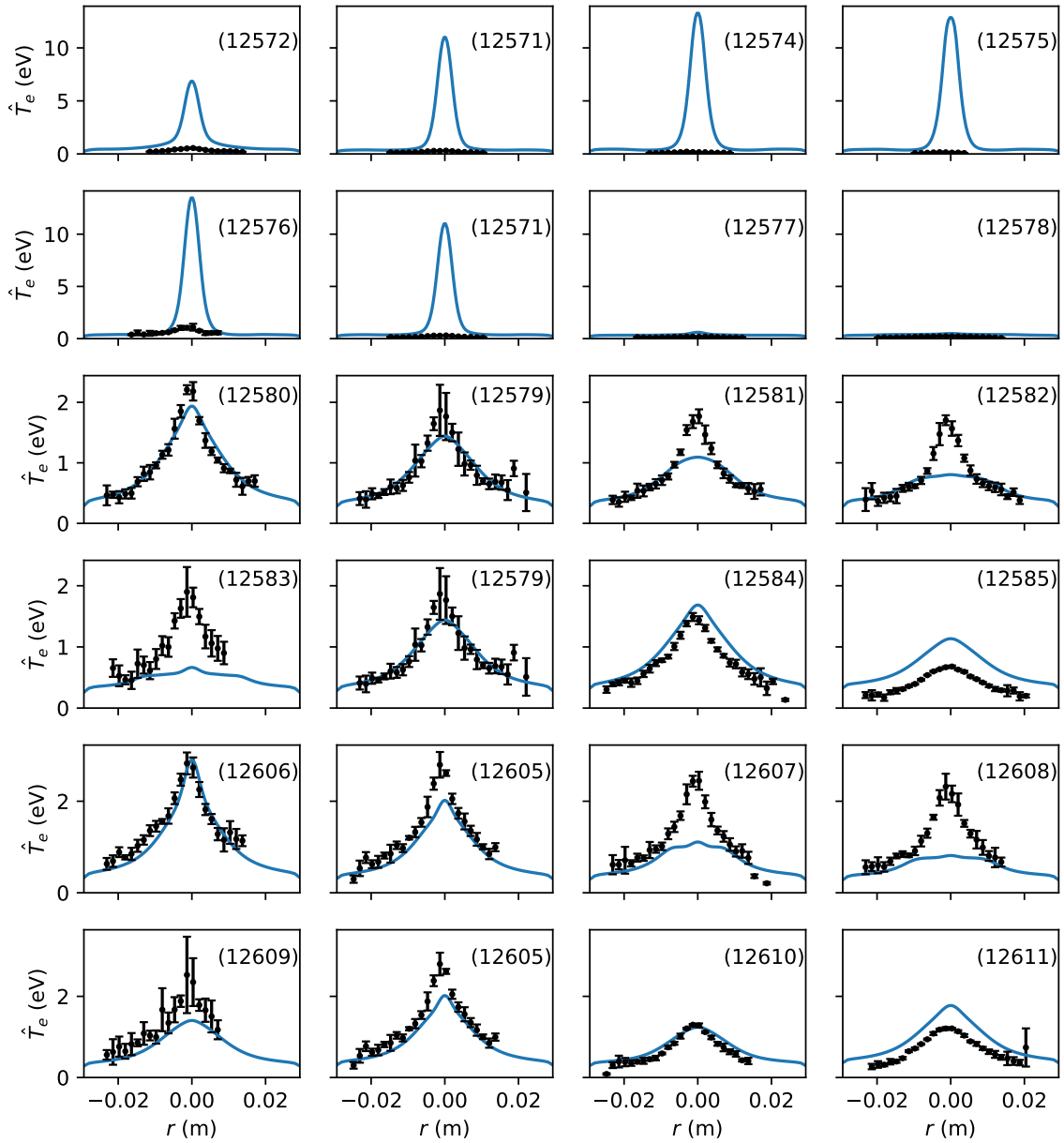

Figure 23: Electron temperature in front of the target (at $z = 0$ m) compared to model predictions for all 21 discharges in Table 4, there are three duplicates in the second column for ease of comparing rows. All TS readings were 29.2 mm from the target, the pumping power was set to 82% of max capacity and the target potential was floating. The first two rows are at a magnetic field strength of 0.4 T, the third and fourth row are at 0.8 T and the last two at 1.2 T. In the first, third and fifth row the gas flow is scanned, in the second, fourth and sixth row the current is scanned. Each panel in the same row has the same y-axis. Lastly, the TS# is indicated in the corners.

Acknowledgements
Firstly, I'd like to thank my supervisors Hugo de Blank, Peter Rindt and Jan van Dijk. Their door was always open for questions, also they were very helpful in giving feedback. Secondly I'd like to express my appreciation to the TU/e fusion group and the Differ community for their assistance. Specifically I want to thank Ray Chandra for helping out with questions I had regarding plasma modelling, Gijs Akkermans for his help with the experiments, and Karol Ješko for his perspective on simulation issues that I ran into. Furthermore the Magnum-PSI team was very helpful in arranging the experiment and explaining the diagnostics. Lastly, I want to thank SURFsara for their computing time.